International Journal of Heat and Fluid Flow xxx (2011) xxx–xxx

Contents lists available at ScienceDirect

International Journal of Heat and Fluid Flow

journal homepage: www.elsevier.com/locate/ijhff

DNS of buoyancy-driven flows and Lagrangian particle tracking in a square cavity at high Rayleigh numbers

R. Puragliesi [a,b], A. Dehbi [a,*], E. Leriche [c], A. Soldati [d], M.O. Deville [b]

[a] Nuclear Energy and Safety Research Department, Paul Scherrer Institut, CH-5232 Villigen PSI, Switzerland
[b] Laboratoire d'Ingénierie Numérique, École Polytechnique Fédérale de Lausanne, Station 9, CH-1015 Lausanne, Switzerland
[c] Université de Lyon, F-42023 Saint-Étienne, LMFA@UJM St-Étienne, CNRS UMR 5509 Université de St-Étienne, 23 rue Docteur Paul Michelon, F-42023 Saint-Étienne, France
[d] Dipartimento di Energetica e Macchine, Università di Udine, Via delle Scienze 208, IT-33100 Udine, Italy

ARTICLE INFO

Article history:
Received 16 April 2010
Received in revised form 11 April 2011
Accepted 15 June 2011
Available online xxxx

Keywords:
Natural convection
DNS
Particle deposition
Enclosure
Aerosol

ABSTRACT

In this work we investigate numerically particle deposition in the buoyancy driven flow of the differentially heated cavity (DHC). We consider two values of the Rayleigh number ($Ra = 10^9, 10^{10}$) and three values of the particle diameter ($d_p = 15, 25, 35$ [μm]). We consider the cavity filled with air and particles with the same density of water $\rho_w = 1000$ [kg/m^3] (aerosol). We use direct numerical simulations (DNS) for the continuous phase, and we solve transient Navier–Stokes and energy transport equations written in an Eulerian framework, under the Boussinesq approximation, for the viscous incompressible Newtonian fluid with constant Prandtl number ($Pr = 0.71$). First- and second-order statistics are presented for the continuous phase as well as important quantities like turbulent kinetic energy (TKE) and temperature variance with the associated production and dissipation fields. The TKE production shows different behaviour at the two Rayleigh numbers.

The Lagrangian approach has been chosen for the dispersed phase description. The forces taken into account are drag, gravity, buoyancy, lift and thermophoresis. A first incursion in the sedimentation mechanisms is presented. Current results indicate that the largest contribution to particle deposition is caused by gravitational settling, but a strong recirculating zone, which liftoffs and segregates particles, contributes to decrease settling. Deposition takes place mostly at the bottom wall. The influence of lift and thermophoretic forces on particle removal is discussed in detail. Indeed, it is shown that the lift is responsible of particle deposition on the vertical cold surface.

© 2011 Elsevier Inc. All rights reserved.

1. Introduction

In present years the upcoming problems concerning energy production and environmental pollution have driven research efforts in different aspects of nuclear energy production processes and nuclear power plant safety. Extensive experimental campaigns and numerical studies (Clément et al., 2003; Guentay et al., 2004; Kissane, 2008) have been performed to assess the risks and the environmental impact of a nuclear severe accident. One of the major issues in a severe accident scenario is to predict with accuracy the deposition rate and the removal mechanisms of micro-size aerosol particles driven by natural convective flows inside large containments. This has motivated the present research, the object of which is to understand the role of natural convective chaotic flows in particle segregation and depletion phenomena inside air-filled enclosure. To model the problem we focus our attention on a simplified geometry, a square domain, where the vertical walls are kept at two different temperatures, the horizontal walls are adiabatic and the fluid motion is induced by local differences of density. Together with a statistical analysis of the chaotic flow regime, we also provide a first investigation in particle transport mechanisms in the so-called two-dimensional (2D) differentially heated cavity (DHC).

The DHC is a well known 2D numerical benchmark initially stated in de Vahl Davis (1983) and de Vahl Davis and Jones (1983). Hereafter a non-exhaustive literature review is provided. Since the pioneering work conducted by de Vahl Davis (1983) and de Vahl Davis and Jones (1983), who investigated flows for values of the Rayleigh number ranging from 10^3 up to 10^6 in the laminar case, LeQuéré (1991) presented very accurate solutions for $10^6 \leqslant Ra \leqslant 10^8$ in the laminar regime employing pseudo-spectral Chebyshev collocation method to solve the Navier–Stokes and energy transport equations written in primitive variables under the Boussinesq approximation. Noteworthy findings are the centro-symmetry property of the temperature and velocity fields, the

* Corresponding author.
E-mail addresses: riccardo.puragliesi@psi.ch (R. Puragliesi), abdel.dehbi@psi.ch (A. Dehbi), emmanuel.leriche@univ-st-etienne.fr (E. Leriche), soldati@uniud.it (A. Soldati), michel.deville@epfl.ch (M.O. Deville).

0142-727X/$ - see front matter © 2011 Elsevier Inc. All rights reserved.
doi:10.1016/j.ijheatfluidflow.2011.06.007

Please cite this article in press as: Puragliesi, R., et al. DNS of buoyancy-driven flows and Lagrangian particle tracking in a square cavity at high Rayleigh numbers. Int. J. Heat Fluid Flow (2011), doi:10.1016/j.ijheatfluidflow.2011.06.007

detachment regions at the horizontal adiabatic walls and the large zone of linear thermal stratification of the central core region. For increasingly higher Rayleigh numbers the flow eventually becomes unsteady. LeQuéré and Behnia (1998) conducted 2D DNS calculations around the transitional regime up to $Ra = 10^{10}$. They identified the critical Rayleigh number $Ra^c = 1.82 \times 10^8$ The onset of the first transition to periodicity and the physical description of the instability mechanism are still an open question (Paolucci and Chenoweth, 1989; Ravi et al., 1994; Janssen and Henkes, 1996). First- and second-order time-averaged statistics of velocity and temperature fields, *turbulent* kinetic energy and temperature variance and the respective dissipation fields have been also reported in LeQuéré and Behnia (1998).

In Ravnik et al. (2006), Podvin and Le Quéré (2001), Gelfgat (2004) and Xin and Le Quéré (2002), the influence on the flow of different aspect ratios of the rectangular cavity have been examined. It has been found that for increasing aspect ratios, up to five, the critical Rayleigh number decreases. Two-dimensional simulations with a non-Boussinesq fluid can be found in Suslov and Paolucci (1997), Suslov and Paolucci (1995) and LeQuéré et al. (1992) for the laminar regime. With this kind of fluid the centro-symmetry property of the flow is not preserved and the transition to unsteadiness occurs at lower Rayleigh number with respect to the Boussinesq case. A direct comparison with published experimental results has always been difficult due to critical differences in the thermal boundary conditions at the horizontal walls imposed experimentally (Ampofo and Karayannis, 2003; Mamun et al., 2003; Leong et al., 1999; Leong et al., 1998; Mergui and Penot, 1997; Tiang and Karayiannis, 2000b; Tiang and Karayiannis, 2000a).

The transport of heavy particles has been the object of numerous experimental and numerical studies (for a review (Elghobashi, 1994; Gouesbet and Berlemont, 1998; Soldati, 2005)), but there is a deep lack of knowledge in segregation and sedimentation processes inside closed cavities. In Tsorng et al. (2006) and Tsorng et al. (2008), stereo imaging and signal processing techniques are used to reconstruct and visualize the pathlines of macroscopic neutrally buoyant particles in three-dimensional lid driven cavity flow at low Reynolds number ($Re = 470$). Spiral motions from the mid plane to the sidewalls and back are depicted and particle fluid structure selectivity is also encountered. In Allery et al. (2008), proper orthogonal decomposition (POD) of the relevant fluid flow modes based on LES computation is coupled with a Lagrangian particle tracker that uses standard Runge–Kutta method for the integration of the particle equation of motion (PEM). Yarin et al. (1996) have observed numerically and experimentally inertial particles trajectories in a cubic DHC at laminar regime of a non-Boussinesq fluid. Interesting results are particle trapping close to the hot wall and spiral motions from the side walls to the midplane and vice versa. Finally, Akbar et al. (2009) have studied the behaviour of sub-micron particles in a laminar DHC with a non-Boussinesq fluid using finite volume space discretization. Their major finding is that thermophoretic force and Brownian diffusion are the most efficient mechanisms that rule the removal process of sub-micron particles.

In the present work, three different sets of particles of density $\rho_w = 1000$ [kg/m^3] and diameter $d_p = 15, 25, 35$ [μm] have been randomly injected in a square cavity filled with air ($Pr = 0.71$) at standard thermodynamic room conditions ($T_R = 293.15$ [K], $p_R = 101{,}325$ [Pa]). With the objective of obtaining a better understanding of the dynamics that governs the particle deposition in natural convective flows at high Rayleigh number ($Ra = 10^9$, 10^{10}), time-dependent Navier–Stokes and energy transport equations are solved using DNS. A second-order time accurate scheme and a pseudo-spectral Chebyshev collocation method has been chosen as the most suitable numerical methodology yielding high spatial accuracy, low numerical diffusion and fast convergence at reasonable computational costs. The reader should be aware that the following statistical analysis of the 2D flow provides information that is not truly related to the actual turbulent natural convective flow which is intrinsically three-dimensional. Anyway, the reported quantities have to be interpreted as a good approximation of the global behaviour natural convective flows undergo when increasing the governing parameter *Ra* since the contribution of spanwise fluctuations to turbulent quantities is small in the regime here considered (Puragliesi, 2010). Moreover, in the DHC configuration, the stabilizing action of the thermal stratification inhibits the development of large homogeneous chaotic regions so that the computed fluctuating quantities are only locally significant and show high anisotropy since yet strongly linked to the mean large flow scales.

The aerosol swarms are tracked using Lagrangian approach in the assumption of one-way coupling: a 6th-order Lagrange spatial interpolation (Section 2.2) is used to locally evaluate the fluid quantities at the particle position and standard 4th-order explicit Runke–Kutta (ERK4) method is employed in order to time integrate the particle trajectory.

2. Methodology

2.1. Continuous fluid phase

The square domain of edge-length H and the imposed boundary conditions are schematised in Fig. 1. The two vertical opposite walls are kept at different constant temperature, T_H and T_C are the hot and cold wall temperatures respectively, whereas the horizontal walls are assumed adiabatic. No-slip condition for the fluid velocity is applied to all the cavity solid boundaries. The fluid considered, *i.e.* air, is assumed homogeneous, incompressible, Newtonian with uniform (in space) and constant (in time) kinematic viscosity ν_R and thermal diffusivity κ_R (the subscript R indexes quantities that are measured at the reference temperature $T_R = \frac{T_H + T_C}{2}$). The temperature difference $\Delta T = T_H - T_C$ is supposed to be sufficiently small to fulfil the Oberbeck-Boussinesq approximation (Gray and Giorgini, 1976; Niemela and Sreenivasan, 2006). According to Bejan (1984) and LeQuéré (1991), the appropriate scaling quantities for velocity, length, time and pressure in natural convection with $Pr \approx 1$ are

$$U^* = \frac{\kappa_R}{H}\sqrt{Ra}, L^* = H, t^* = \frac{H^2}{\kappa_R\sqrt{Ra}}, P^* = \rho_R U^{*2}. \quad (1)$$

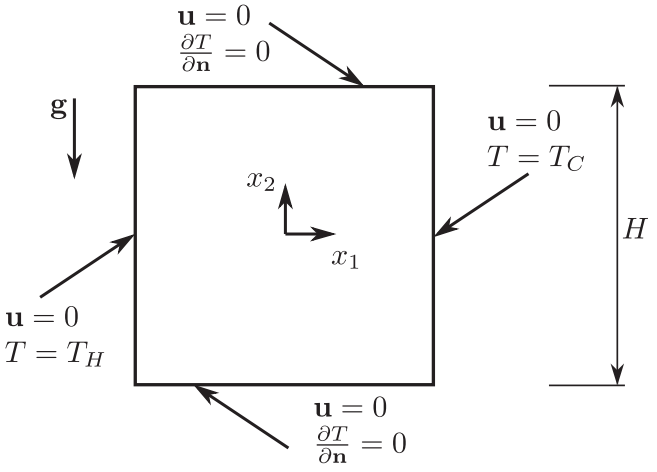

Fig. 1. Schematic geometry representation and boundary conditions.

Please cite this article in press as: Puragliesi, R., et al. DNS of buoyancy-driven flows and Lagrangian particle tracking in a square cavity at high Rayleigh numbers. Int. J. Heat Fluid Flow (2011), doi:10.1016/j.ijheatfluidflow.2011.06.007

where the Rayleigh number Ra is defined as

$$Ra = \frac{g\alpha_R \Delta T H^3}{\kappa_R \nu_R}. \quad (2)$$

The velocity scaling is proportional to the maximum velocity of the vertical jets. From a numerical viewpoint, at high Rayleigh numbers this choice relaxes the limitation on the integration time-step when employing explicit/semi-explicit discretization time-schemes in comparison with scaling based on the thermal or velocity diffusion (de Vahl Davis, 1983; de Vahl Davis and Jones, 1983). Taking into account the Boussinesq approximation and neglecting radiation effects and the power dissipated by the internal viscous stresses, the dimensionless Navier–Stokes equations read in vector notation

$$\frac{\partial \mathbf{u}}{\partial t} + \mathbf{u}\cdot\nabla\mathbf{u} = -\nabla p + \frac{Pr}{\sqrt{Ra}}\Delta\mathbf{u} - Pr\Theta\frac{\mathbf{g}}{|\mathbf{g}|} \quad (3)$$

$$\nabla\cdot\mathbf{u} = 0 \quad (4)$$

$$\frac{\partial \Theta}{\partial t} + \mathbf{u}\cdot\nabla\Theta = \frac{1}{\sqrt{Ra}}\Delta\Theta \quad (5)$$

with the following boundary conditions for velocity and temperature

$$\mathbf{u}(x_1 = \pm 0.5, x_2) = \mathbf{0} \text{ for all } x_2 \in [-0.5, +0.5] \quad (6)$$

$$\mathbf{u}(x_1, x_2 = \pm 0.5) = \mathbf{0} \text{ for all } x_1 \in [-0.5, +0.5] \quad (7)$$

$$\Theta(x_1 = \pm 0.5, x_2) = \mp 0.5 \text{ for all } x_2 \in [-0.5, +0.5] \quad (8)$$

$$\frac{\partial \Theta}{\partial x_2}(x_1, x_2 = \pm 0.5) = 0 \text{ for all } x_1 \in [-0.5, +0.5] \quad (9)$$

where the position vector is $\mathbf{x} := (x_1, x_2)$, the velocity vector is $\mathbf{u} := (u_1, u_2)$, $Pr = \nu_R/\kappa_R$ is the Prandtl number and the dimensionless temperature $\Theta = (T - T_R)/\Delta T$. A complete overview of the physical properties and other parameters considered in the present work is given in Table 1.

The initial velocity distribution is set to zero and the initial temperature distribution is given by a linear distribution between the cold and the hot walls if $Ra < Ra^c$, otherwise a solution computed at the immediate lower Rayleigh number is used for saving computing time and numerical stability reasons.

The spatial approximation of any field relies on the expansion in tensor product of Chebyshev polynomials of order N along every space direction and a usual collocation method is applied at the Chebyshev-Gauss–Lobatto (CGL) points (Gottlieb and Orszag, 1977; Canuto et al., 1988). The projection-diffusion method introduced in Batoul et al. (1994), which imposes the incompressibility constraint by decoupling the velocity and pressure computation, is chosen for its consistency with the continuous space–time problem and for its optimal cost. The pressure is expanded into polynomials of the same order as the velocity, while intermediate velocity components are truncated in a way that enforces continuity without any contamination by spurious pressure modes (Labrosse, 1993). A complete numerical analysis of this decoupling method may be found in Leriche and Labrosse (2000) and Leriche et al. (2006) where it is compared with the high-order time splitting scheme proposed by Karniadakis et al. (1991).

Table 1
Air physical properties and other parameters.

Reference temperature	T_R	293.15	[K]
Temperature difference	ΔT	42.97	[K]
Reference density	ρ_R	1.20	[kg m^{-3}]
Kinematic viscosity	ν_R	1.51×10^{-5}	[m^2 s^{-1}]
Thermal diffusivity	κ_R	2.12×10^{-5}	[m^2 s^{-1}]
Prandtl number (ν_R/κ_R)	Pr	0.71	[–]
Thermal expansion coefficient	α_R	3.41×10^{-3}	[K^{-1}]
Gravity acceleration	$\|\mathbf{g}\|$	9.81	[m s^{-2}]

Table 2
Benchmark results for $Ra = 10^7$.

Quantity	Present work	LeQuéré (1991)	Tric et al. (2000)
N	129	81	51
$\|u_1\|_{max}$	0.1229100	n.a.	n.a.
(x_1, x_2)	(0.3770909, −0.4661157)	n.a.	n.a.
$\|u_1\|_{0,max}$	0.0468686	0.046986	0.047
(x_2)	(0, −0.3793228)	(0, 0.379)	(0, 0.379)
$\|u_2\|_{max}$	0.2217788	n.a.	n.a.
(x_1, x_2)	(0.4793333, 0.0349471)	n.a.	n.a.
$\|u_2\|_{0,max}$	0.2211476	0.221118	0.221
(x_1)	(0.4786996, 0)	(0.479, 0)	(0.479, 0)
$\|\Psi\|_{max}$	9.5387249×10^{-3}	9.5387×10^{-3}	n.a.
(x_1, x_2)	(0.4139739, −0.0555289)	(−0.414, 0.056)	n.a.
$\|\Psi\|_0$	9.2849611×10^{-3}	9.2850×10^{-3}	n.a.
$\overline{Nu}_h$	16.52309	16.523	16.522
$\overline{Nu}_m$	16.52309	16.523	16.522

The time discretization of the Navier–Stokes and energy equations is based on a second-order backward Euler differentiation formula. The diffusive terms in the momentum Eq. (3) and in the energy Eq. (5) are treated implicitly, whereas the advective terms are advanced explicitly in time by a second-order extrapolation scheme. The overall accuracy is second-order in time and the scheme is subject to restrictions in the time step due to the explicit advancement of the advective terms (Deville et al., 2002). The form of the discretized equations is represented by a vectorial Helmholtz system for the velocity, a quasi-Poisson operator for the pressure, and a scalar Helmholtz equation for the temperature that need to be solved at each time step. A fast diagonalisation method is used for inverting these elliptic operators at a low computational cost (Lynch et al., 1964; Haldenwang et al., 1984). The code has been benchmarked with results previously presented in the literature for the laminar regime. In Table 2 several local and integral quantities are compared with those in LeQuéré (1991) and Tric et al. (2000). The positions of the maxima are obtained by using Newton–Raphson technique on the CGL grid coupled with spectral interpolation for the field quantities and derivatives, whereas integral quantities are computed using spectral integration. N is polynomial degree in each space direction, $|u_i|_{max}$ is the maximum absolute value of the velocity component u_i and (x_1, x_2) its position, $|u_i|_{0,max}$ is the maximum absolute value of the velocity component u_i along the horizontal (if $i = 2$) or vertical (if $i = 1$) centre-line, (x_i) their position along the centre-lines, $|\Psi|_{max}$ is the maximum absolute value of the stream-function and (x_1, x_2) its position, $|\Psi|_0$ the absolute value of the stream-function at the centre of the cavity, finally the space averaged Nusselt number at the hot wall $\overline{Nu}_H$ and the vertical centre-line $\overline{Nu}_M$. The local Nusselt number is defined as follows

$$\mathbf{Nu} := -\nabla\Theta + \sqrt{Ra}\mathbf{u}\Theta \quad (10)$$

while its space average along a line $\mathscr{L}$, lying on the plane (x_1, x_2), of length L, with unit normal vector $\mathbf{n}$ and $0 \leqslant s \leqslant L$ the curvilinear coordinate, is given by

$$\overline{Nu}_L = \frac{1}{L}\int_L \mathbf{Nu}_{\mathscr{L}}(s)\cdot\mathbf{n}\, ds. \quad (11)$$

More benchmark cases and details can be found in Puragliesi (2010).

2.2. Dispersed aerosol phase

In the present work three sets of randomly space distributed particles with diameter $d_p = 15$, 25, 35 [μm] and density $\rho_w = 1000$ [kg/m^3], each one counting $N_p = 10^5$ pointwise, rigid spheres, are separately injected inside the cavity when the flow

Please cite this article in press as: Puragliesi, R., et al. DNS of buoyancy-driven flows and Lagrangian particle tracking in a square cavity at high Rayleigh numbers. Int. J. Heat Fluid Flow (2011), doi:10.1016/j.ijheatfluidflow.2011.06.007

Table 3
Computational parameters: polynomial degree N, minimum and maximum grid size Δx_i, integration time step Δt, number of frames per unit of time and averaging time.

Ra	N	$min(\Delta x_i)$	$max(\Delta x_i)$	Δt	Sampl. freq.	Ave. time
10^9	257	3.8×10^{-5}	6.1×10^{-3}	2.5×10^{-3}	10	1050.0
10^{10}	321	2.4×10^{-5}	5.0×10^{-3}	1.0×10^{-3}	20	1760.0

is already developed and statistically steady. In this work the volume fraction is sufficiently low to neglect particle–fluid momentum and energy transfer, and particle–particle interaction (i.e. collisions). The fluid density, ρ, is locally given by the Boussinesq approximation $\rho = \rho_R(1 - \alpha_R \Delta T \Theta)$ with α_R being the thermal expansion coefficient of the fluid, see Table 1. Under the above assumptions the important forces acting on spherical particles are drag, gravity and buoyancy (Elghobashi and Truesdell, 1992). However, since we aim to clarify also the role of second-order effects on the particle dynamics due to local gradients of velocity and temperature, which are maximum through the vertical boundary layers and scale with $Ra^{1/4}$, we will use the following modified Basset-Boussinesq-Oseen equation (Gatignol, 1983)

$$\frac{d\mathbf{x}_p}{dt} = \mathbf{v}_p \tag{12}$$

$$\frac{d\mathbf{v}_p}{dt} = \underbrace{\frac{f}{St}(\mathbf{u} - \mathbf{v}_p)}_{\text{Drag}} \times \underbrace{-\frac{Pr}{\Delta\mathscr{T}}[1 - \mathscr{D}(1 - \Delta\mathscr{T}\Theta)]\mathbf{e}_2}_{\text{Buoyancy}} + \underbrace{\mathscr{D}C_L[(\mathbf{u} - \mathbf{v}_p) \times \boldsymbol{\omega}]}_{\text{Lift}} \times \underbrace{-2C_T \frac{Pr\Delta\mathscr{T}}{St\sqrt{Ra}} \frac{\nabla\Theta}{1 - (\Delta\mathscr{T}\Theta)^2}}_{\text{Thermophoresis}}. \tag{13}$$

where $\mathbf{x}_p$ and $\mathbf{v}_p$ are the particle dimensionless position and velocity respectively, $f = \left(1 + 0.15Re_p^{0.687}\right)$ represents the drag correction coefficient which applies when the particle Reynolds number

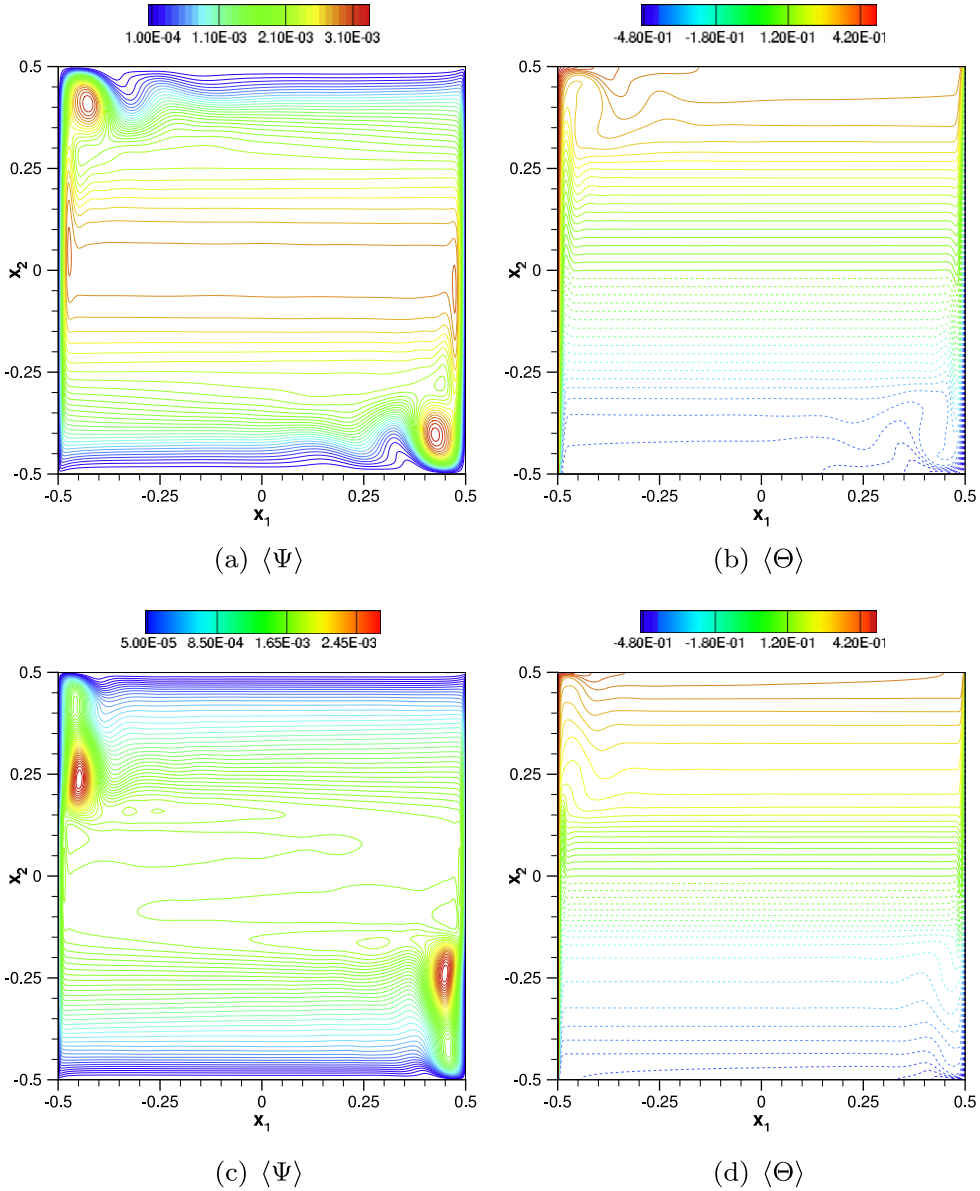

(a) $\langle\Psi\rangle$ (b) $\langle\Theta\rangle$

(c) $\langle\Psi\rangle$ (d) $\langle\Theta\rangle$

Fig. 2. Time-averaged stream-functions $\langle\Psi\rangle$ and temperature fields $\langle\Theta\rangle$. In (a and b), results for $Ra = 10^9$ and (c and d) results for $Ra = 10^{10}$.

Please cite this article in press as: Puragliesi, R., et al. DNS of buoyancy-driven flows and Lagrangian particle tracking in a square cavity at high Rayleigh numbers. Int. J. Heat Fluid Flow (2011), doi:10.1016/j.ijheatfluidflow.2011.06.007

$Re_p = \rho\ d_p|\mathbf{u} - \mathbf{v}_p|/(\rho_R \nu_R)$ exceeds the unity,[1] the particle Stokes number is given by

$$St = d_p^2/(18\mathscr{D}\nu_R t^*), \tag{14}$$

$\mathbf{e}_2$ is the vertical upward unit vector (opposite to $\mathbf{g}$ in Fig. 1), $\mathscr{D} = \rho_R/\rho_w$ is the fluid to particle density ratio, $\Delta\mathscr{T} = \alpha_R \Delta T$ is the dimensionless temperature difference and $\boldsymbol{\omega} = \nabla \times \mathbf{u}$ refers to the dimensionless local fluid vorticity. For the definition of the coefficients C_L and C_T refer to Cherukat et al. (1999), Kurose and Komori (1999), Giusti et al. (2005) and Talbot et al. (1980).

The particle velocity at the injection time is set equal to the fluid velocity at the particle position and perfect absorbing wall condition is imposed at the solid boundaries. This implies that when particles collide at the walls they stick and do not re-enter in the core domain because of rebounce or lubrication effects. In order to evaluate the forces acting on particles at their instantaneous positions, fluid velocity and fluid temperature are required. Balachandar and Maxey (1989) and Kontomaris et al. (1992) showed that 6th-order Lagrangian interpolation gives sufficiently accurate results on Lagrangian statistics of homogeneous isotropic turbulence. Thus the nodal fluid quantities are locally interpolated using a sixth-order Lagrange interpolator. However, preliminary comparison between full Chebyshev interpolation and the Lagrange polynomial interpolation has been conducted to validate the proposed method: no relevant discrepancies have been recorded. Further, Eqs. (12) and (13) are time integrated with a standard explicit fourth-order Runge–Kutta scheme (ERK4).

3. Results and discussion

3.1. Continuous phase

Two different cases at $Ra = 10^9$, 10^{10} are analysed in terms of first- and second-order statistical moments and budgets. These quantities are related to the chaotic, random processes yielded by the non-linear nature and instability of the Navier–Stokes–Boussinesq equations Eq. (3)–(5). A summary of the computational parameters is provided in Table 3. The ratio of the smallest to the highest spectral coefficient ($\leqslant O(10^{-5})$) and the residuals of the time-averaged momentum and energy equations ($\leqslant O(10^{-5})$) have been used as convergence criteria (Puragliesi, 2010).

3.1.1. First-order moments

According to the Reynolds decomposition, instantaneous statistically steady random variable of time and space $\phi(\mathbf{x},t)$ can be easily described as the sum of its mean value in time $\langle\phi(\mathbf{x})\rangle$ and its fluctuating component $\phi'(\mathbf{x},t)$, resulting in [2]

$$\phi(\mathbf{x},t) = \langle\phi(\mathbf{x})\rangle + \phi'(\mathbf{x},t). \tag{15}$$

In the following all the quantities indicated with $\langle\cdot\rangle$ and $\cdot'$ represent the time-averaged and fluctuating parts of the field under investigation.

In Fig. 2 the time-averaged stream-function $\langle\Psi\rangle$ and temperature $\langle\Theta\rangle$ fields are shown for $Ra = 10^9$, 10^{10}. The distinct characteristic mean flow structures appearing at the two regimes are two separate velocity and thermal boundary layers at the vertical active walls whose thickness scales with $Ra^{-1/4}$, two primary counter flows along the external part of the vertical boundary layers, two recirculating pockets (located in the corner regions at $Ra = 10^9$, but shifted upstream at $Ra = 10^{10}$), the hook-like structures (defined later in the text), the temperature stratification in the core region and the global centro-symmetry of the mean velocity and temperature fields. The hook-like structure is schematically illustrated in Fig. 3. The structure itself refers to the high curvature streamlines that turn around one recirculation pocket and diffuses in the upper or lower part of the domain. The time-averaged streamlines show clearly that the hook-like structure at $Ra = 10^9$ presents very high curvature between the recirculation pocket (also commonly called corner-eddy) and the primary counterflow outside the vertical boundary layer, whereas for $Ra = 10^{10}$ the highest curvature occurs where the fluid turns due to the presence of the horizontal adiabatic wall. For the highest Rayleigh number considered in the present work, we can observe the formation of secondary counter-rotating horizontal flows in the core region (see Fig. 2b). This behaviour is a departure from the slightly *turbulent* regimes previously published in the literature with adiabatic horizontal walls even if it was detected at lower Rayleigh numbers in Peng and Davidson (2001) and other works where linear or experimental temperature profiles have been imposed at the horizontal walls. In these latter configurations, the earlier appearance of such a flow pattern can be explained with the presence of Rayleigh-Bénard instabilities in the horizontal boundary layers that are absent in the adiabatic case. Finally, at $Ra = 10^{10}$ we can notice that the core temperature linear stratification gets narrowed due to the enhanced *turbulent* mixing which enlarges the almost isothermal upper and lower regions close to the adiabatic walls (Fig. 2d).

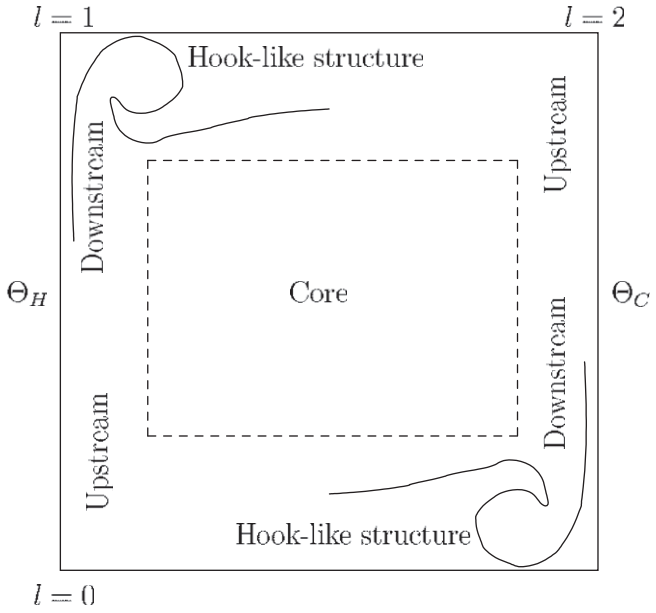

Fig. 3. Schematic representation of the hook-like structure.

In natural convection the pressure field does not govern directly the flow. However in the present configuration the pressure gradient balances the buoyancy far from the walls even at high Rayleigh numbers (Puragliesi, 2010). This result is clearly shown in Fig. 4 where all the budgets of the mean Navier–Stokes equation for the vertical component of velocity are plotted along the vertical centre-line. The mean buoyancy (BT) and pressure gradient (PG) terms are orders of magnitude larger then the others (*i.e.* the convective term (CTM), viscous diffusion (VD) and Reynolds tensor components (RS) are negligible).

In Fig. 5a we show the profile of the time-averaged local shear stress $\langle\tau_w\rangle$ evaluated on the cavity half perimeter length l, starting clockwise from the bottom-left corner up to the top-right one. The mean local shear stress $\langle\tau_w\rangle$ defined at the hot wall as

$$\langle\tau_w\rangle := \frac{Pr}{\sqrt{Ra}}\left(\frac{\partial\langle u_1\rangle}{\partial x_2} + \frac{\partial\langle u_2\rangle}{\partial x_1}\right)_{x_1=-0.5} \tag{16}$$

[1] More precisely if $1 \leqslant Re_p \leqslant 100$.

[2] An estimation of the turnover time is $t_O \approx 20$.

Please cite this article in press as: Puragliesi, R., et al. DNS of buoyancy-driven flows and Lagrangian particle tracking in a square cavity at high Rayleigh numbers. Int. J. Heat Fluid Flow (2011), doi:10.1016/j.ijheatfluidflow.2011.06.007

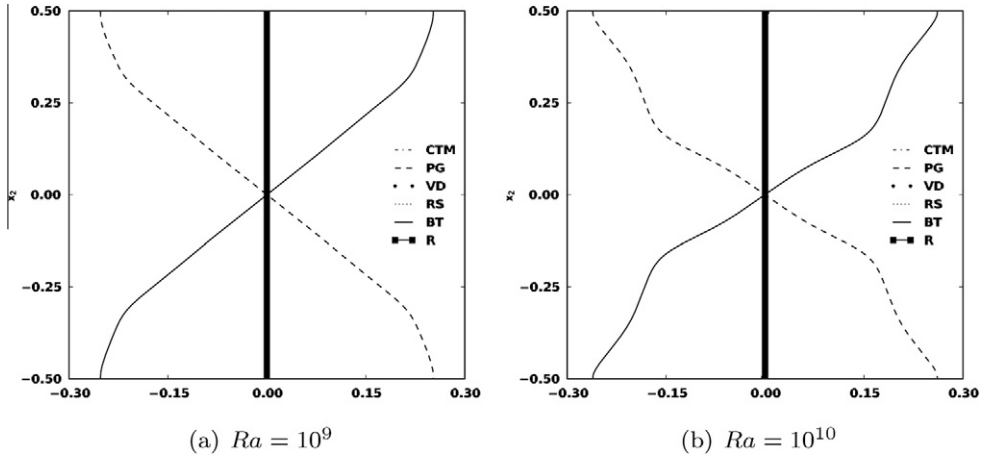

(a) $Ra = 10^9$ (b) $Ra = 10^{10}$

Fig. 4. Time-averaged vertical momentum budgets along the vertical centre-line: (a) for $Ra = 10^9$ and (b) for $Ra = 10^{10}$. Convective Term (CTM), Pressure Gradient (PG), Viscous Diffusion (VD), Reynolds Stresses (RS), Buoyancy Term (BT) and Residual (R).

and at the top adiabatic wall as

$$\langle \tau_w \rangle := \frac{Pr}{\sqrt{Ra}} \left(\frac{\partial \langle u_2 \rangle}{\partial x_1} + \frac{\partial \langle u_1 \rangle}{\partial x_2} \right)_{x_2 = +0.5}. \tag{17}$$

We note that for both Rayleigh numbers the maximum value of $\langle \tau_w \rangle$ occurs before half-height (*i.e.* $l = 0.5$), where the vertical velocity reaches its maximum, and shifts downstream the hot wall for higher *Ra*. An almost linear shear stress region takes place at $0.8 \leqslant l \leqslant 0.9$ where the turbulent flow is developed whereas for $Ra = 10^9$ the linear shear stress region is not clearly recognizable (very narrowed region) indicating that the boundary layer is only weakly *turbulent*, or only in the transition regime. At the top horizontal wall ($1 \leqslant l \leqslant 2$) we observe that, only for the highest Rayleigh number, the mean flow does not present the separation zone, which is identified by zero shear stress for both detachment and re-attachment (Fig. 5a insert).

Concerning the heat transfer at the hot wall, the time averaged local Nusselt number $\langle Nu \rangle = (-\partial \langle \Theta \rangle \partial x_1)_{x_1 = -0.5}$ scaled by $Ra^{-1/4}$ is presented in Fig. 5b. The heat flux has always its maximum at the very beginning of the vertical boundary layer where the mean temperature gradient is high because of the small thickness of the developing laminar boundary layer. For the highest Rayleigh number a local maximum is clearly depicted at $x_2 \approx 0.2$ due to transition to chaotic regime which is not so marked for the case at $Ra = 10^9$. Furthermore, increasing the Rayleigh number leads to a more efficient heat exchange in the last downstream part of the vertical wall. This implies that the enhanced *turbulent* mixing decreases the averaged temperature in the upper (and symmetrically in the lower) part of the domain. One way to identify the extension of the laminar boundary layers at the active walls is to look at the local heat and/or momentum transfer. In fact, the transition region of the vertical boundary layers is characterized by a sudden decrease of the time-averaged shear stress but also by the enhanced convective heat transfer due to the periodic ejection of hot (cold) buoyant pockets which are instantaneously replaced by colder (hotter) fluid coming from the core region. Indeed it appears that the scaling used in this work, *i.e.* $\langle Nu \rangle \propto Ra^{1/4}$, gives good results along the laminar part of the vertical boundary layer. On the other hand, the classical theoretical scaling $Ra^{1/3}$ for developed turbulence should be used in the downstream part of the boundary layer as shown in three dimensional computations (Trias et al., 2010). Trias et al. (2010) showed that an optimal relation for the time- and space-averaged Nusselt number over the active walls is given in the form $\langle \overline{Nu} \rangle = c_1(1 - x_2^{Tr})Ra^{1/3} + c_2 x_2^{Tr} Ra^{1/4}$ (where x_2^{Tr} is the vertical coordinate of the transition point and c_1, c_2 two constants). In this work the latter analysis has not been performed since the flow considered is only 2D but we emphasize that the laminar scaling is not largely affected by the presence of the side walls. From the engineering viewpoint, due to its nature, the DHC is not optimal for studying the asymptotic turbulent heat transfer scaling which is usually performed using time- and space-averaged quantities.

3.1.2. Second-order moments

The mixing induced by the fluctuations of velocity and temperature increases the diffusion of momentum and temperature and withdraws energy from the mean flow to the fluctuating one. In Table 4 the averaged total kinetic energy $\langle e \rangle$, defined as

$$\langle e \rangle = K_T + k_T = \int_\Omega \underbrace{\frac{1}{2} \langle u_i \rangle^2}_{K} d\Omega + \int_\Omega \underbrace{\frac{1}{2} \langle u_i' u_i' \rangle}_{k} d\Omega \tag{18}$$

is reported together with its two components K_T and k_T and relative percentage for both Rayleigh numbers. It is important to emphasize that the fraction of mean kinetic energy k_T contained in the fluctuating field increases sensibly from 11% at $Ra = 10^9$ up to 38% at $Ra = 10^{10}$.

Iso-contours of the turbulent kinetic energy (TKE) distribution *k* at the two Rayleigh numbers are depicted in Fig. 6a and c. The regions of high intensity velocity fluctuations are located inside the recirculating pockets because of the unsteady nature of the hook-like structure. The increase of the Rayleigh number enhances the mixing so that the turbulent kinetic energy diffuses in a wider regions and also it develops upstream the boundary layer, confirming the earlier transition.[3] We note that exists a region where the primary vertical counterflow is subject to a slightly more intense fluctuating activity than the boundary layer which remains laminar. This behaviour could be related to Kelvin–Helmholtz instabilities due to the velocity gradient.

The temperature variance $\langle \Theta' \Theta' \rangle$ iso-contours are shown in Fig. 6b and d. The temperature variance is high close to the vertical boundary layers and its maxima are located around the transition points unlike the TKE. This is related to combined action of the Tollmien-Schlichting waves (Henkes and Hoogendoorn, 1990; Mergui and Penot, 1996; Penot et al., 2010) and the temperature stratification: pockets of hot fluid are transported upward by

[3] The scaling is based on the simple reason that the mass of fluid containing the major amount of energy scales as the laminar boundary layer thickness $\delta \propto Ra^{-1/4}$ in comparison with the total mass of fluid contained in the cavity (Trias et al., 2007).

Please cite this article in press as: Puragliesi, R., et al. DNS of buoyancy-driven flows and Lagrangian particle tracking in a square cavity at high Rayleigh numbers. Int. J. Heat Fluid Flow (2011), doi:10.1016/j.ijheatfluidflow.2011.06.007

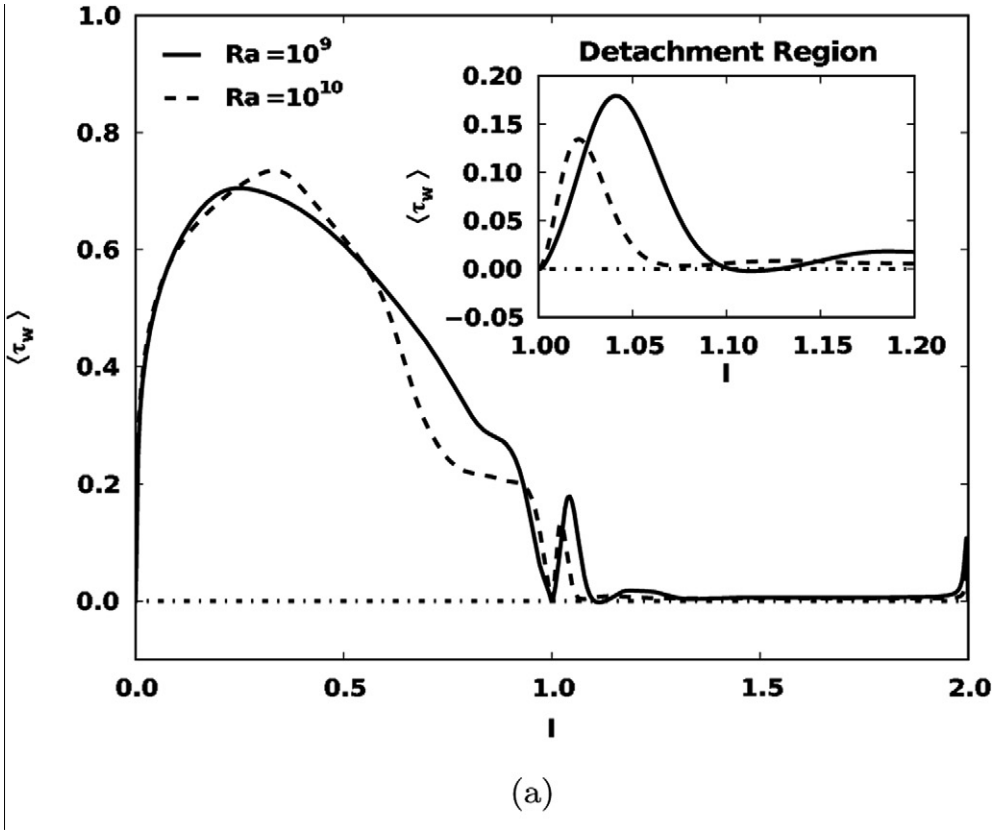

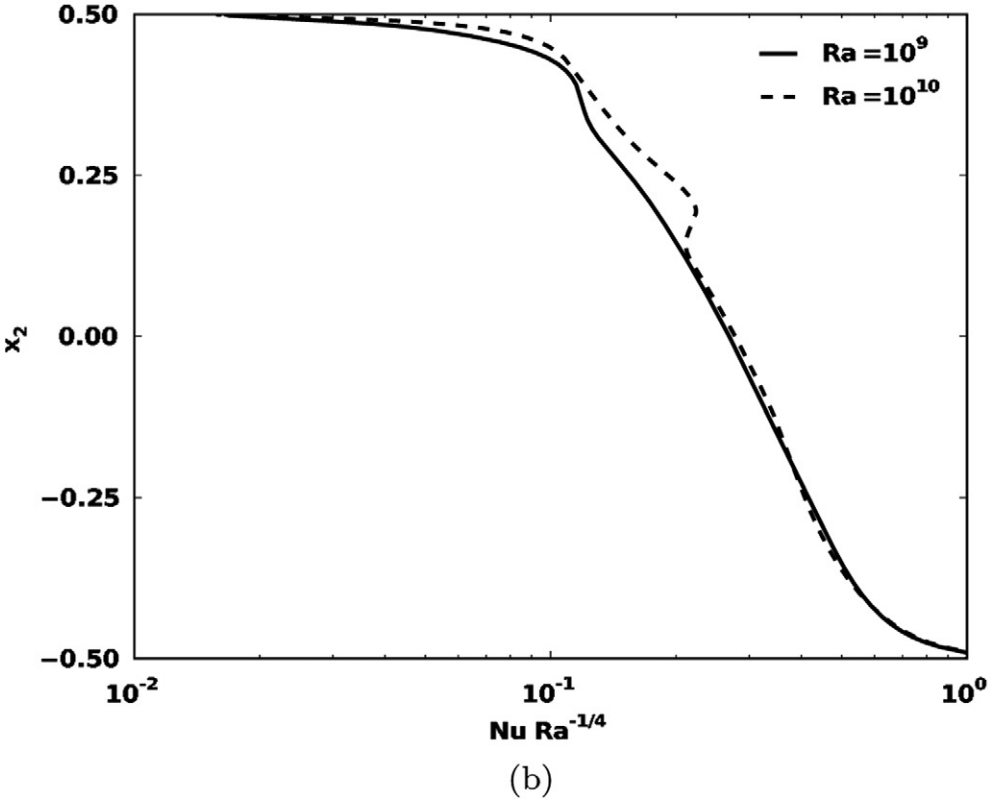

Fig. 5. Momentum and heat flux at the solid boundaries for $Ra = 10^9$ and $Ra = 10^{10}$. (a) Time-averaged local shear stress $\langle \tau_w \rangle$ along the semi-perimeter l. (b) Time-averaged local Nusselt number $\langle Nu \rangle$ at the hot wall.

travelling waves while the cold surrounding fluid replaces them. As the height increases hotter fluid from the core will be sucked so that the temperature fluctuations decrease. It is important to note the wide horizontal temperature variance activity at $Ra = 10^{10}$. This

Please cite this article in press as: Puragliesi, R., et al. DNS of buoyancy-driven flows and Lagrangian particle tracking in a square cavity at high Rayleigh numbers. Int. J. Heat Fluid Flow (2011), doi:10.1016/j.ijheatfluidflow.2011.06.007

can be directly related to the presence of the time-averaged secondary horizontal counterflow that enhances turbulent fluxes of the kind $\langle u_i'\Theta'\rangle$.

According to the transport equation of the mean turbulent kinetic energy

$$\frac{\partial k}{\partial t}+\langle u_j\rangle\frac{\partial k}{\partial x_j}=\frac{\partial}{\partial x_j}\left(\frac{Pr}{\sqrt{Ra}}\frac{\partial k}{\partial x_j}-\langle u_j'k'\rangle-\langle u_j'p'\rangle\right)\underbrace{-\langle u_i'u_j'\rangle\frac{\partial\langle u_i\rangle}{\partial x_j}}_{P}$$
$$\times\underbrace{-\frac{Pr}{\sqrt{Ra}}\left\langle\frac{\partial u_i'}{\partial x_j}\frac{\partial u_i'}{\partial x_j}\right\rangle}_{D}\underbrace{+Pr\langle u_i'\Theta'\rangle\delta_{i,2}}_{G} \qquad (19)$$

the two terms that determine the production (P due to the mean velocity gradient, G due to the buoyancy) and the dissipation rate (D due to the viscous dissipation) are shown in Fig. 7 as a function of $x^- = (x_1+0.5)Ra^{1/4}$ for the elevation $x_2 = +0.3$. Comparing the terms of production P we observe that at $x^-\approx 0.75$ the production term $P_{10}<0$ whereas $P_9>0$ leading to a completely different mechanism of sustainment of k, furthermore for $10\leqslant x^-\leqslant 25$, P_{10} is significantly larger than P_9 (the subscripts refer to the exponents of the two Rayleigh numbers). This behaviour has to be addressed to the fact that, for $Ra = 10^9$, the velocity fluctuations are strongly coupled with the large structures of the flow: the unsteady hook-like structure interacts with the unstable/turbulent boundary layer where the streamlines present very high curvature, whereas this behaviour does not occur at $Ra = 10^{10}$. Concerning the production due to the buoyancy, G, it appears that, for the highest Rayleigh number, this term dissipates the turbulent kinetic energy suggesting that $\langle u_2'\Theta'\rangle<0$. It can be shown that, in a thermally stably stratified medium, a positive vertical displacement of a fluid particle leads to a local negative fluctuation of temperature and vice versa for a negative vertical displacement. This explanation, however, does not apply for $Ra = 10^9$ where G_9 is sightly positive. We can justify this noting that the local vertical temperature profile is neutral or

Table 4
Total averaged specific kinetic energy $\langle e\rangle$ and its mean and fluctuating components K_T and k_T (between brackets the relative percentage) respectively.

Ra	$\langle e\rangle Ra^{1/4}$	$K_T Ra^{1/4}$ (%)	$k_T Ra^{1/4}$ (%)
10^9	0.14862	0.13260(89)	0.01602(11)
10^{10}	0.19283	0.12017(62)	0.07266(38)

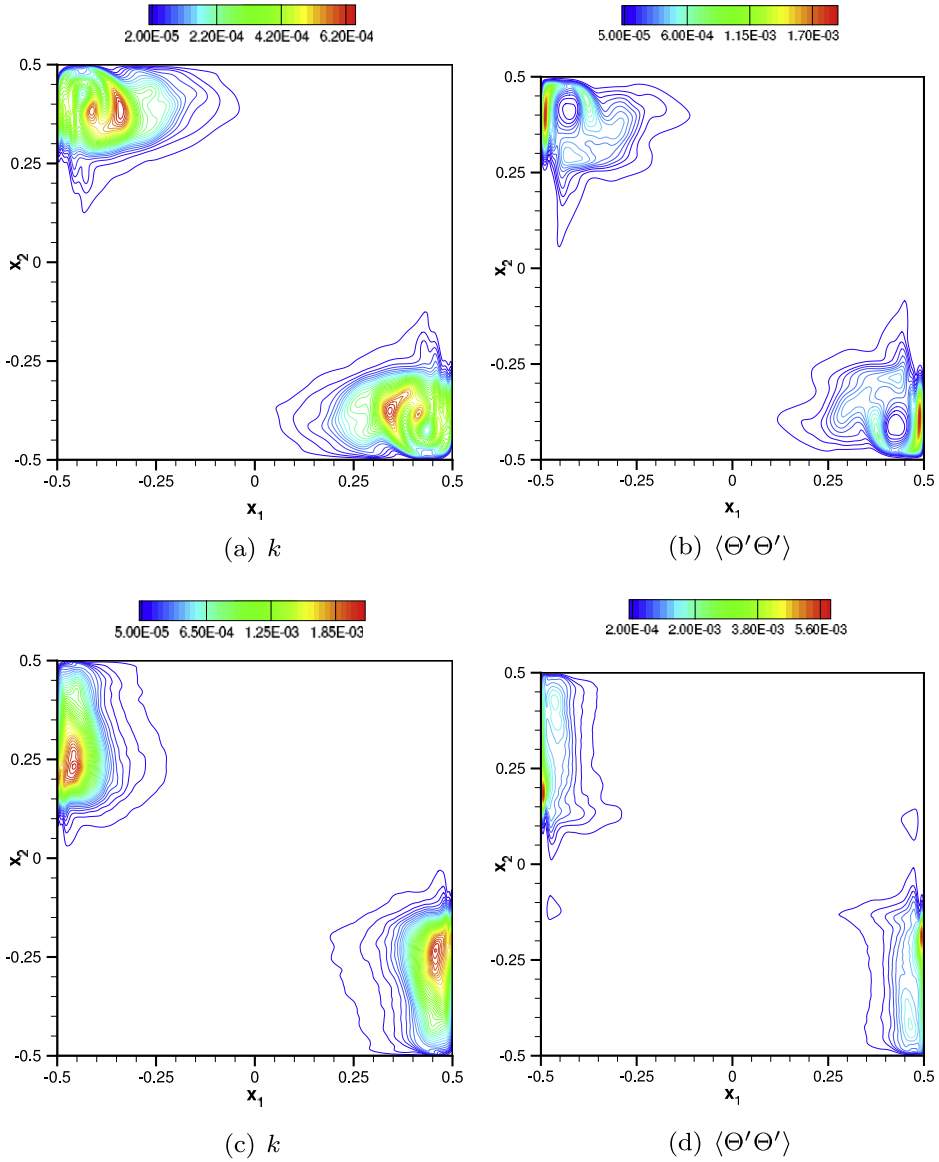

Fig. 6. Turbulent kinetic energy k and temperature variance $\langle\Theta'\Theta'\rangle$ iso-contours: (a and b) for $Ra = 10^9$; (c and d) for $Ra = 10^{10}$.

Please cite this article in press as: Puragliesi, R., et al. DNS of buoyancy-driven flows and Lagrangian particle tracking in a square cavity at high Rayleigh numbers. Int. J. Heat Fluid Flow (2011), doi:10.1016/j.ijheatfluidflow.2011.06.007

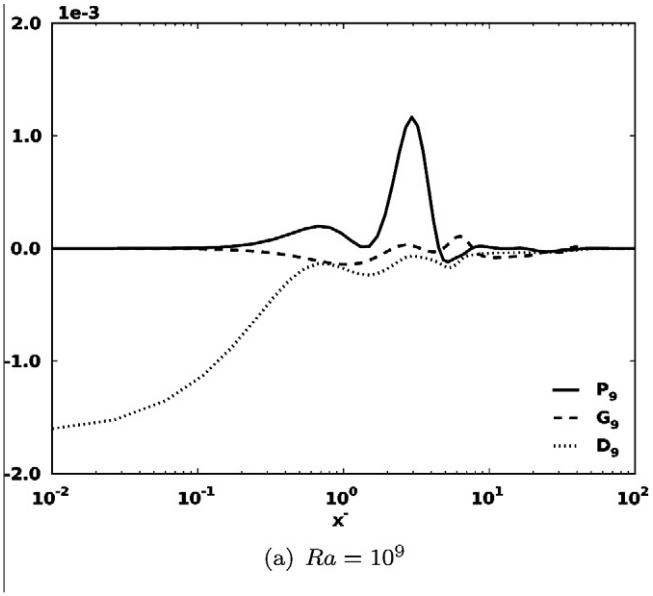

(a) $Ra = 10^9$

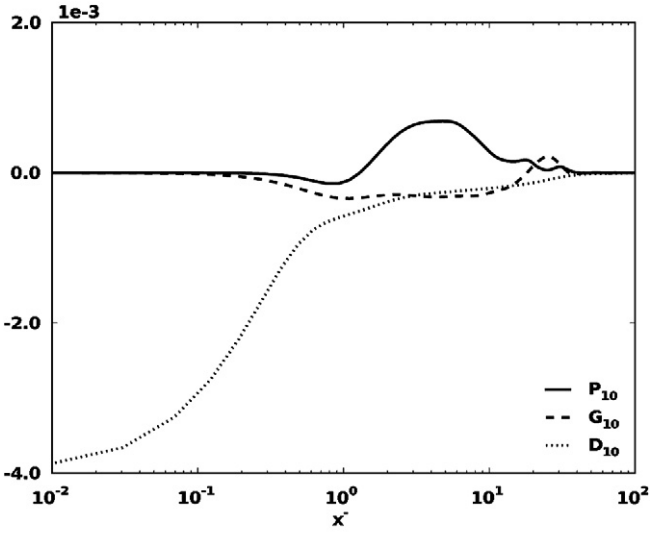

(b) $Ra = 10^{10}$

Fig. 7. Turbulent kinetic energy production (P, G) and dissipation (D) rates at $x_2 = +0.3$ for $Ra = 10^9$, 10^{10}.

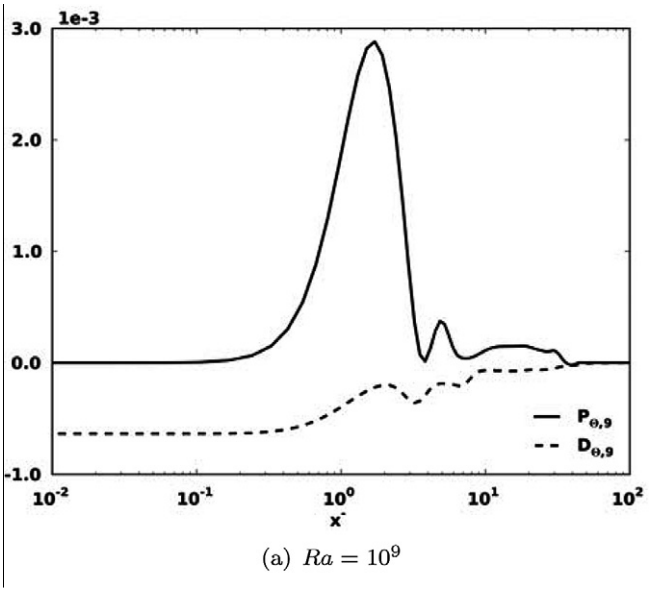

(a) $Ra = 10^9$

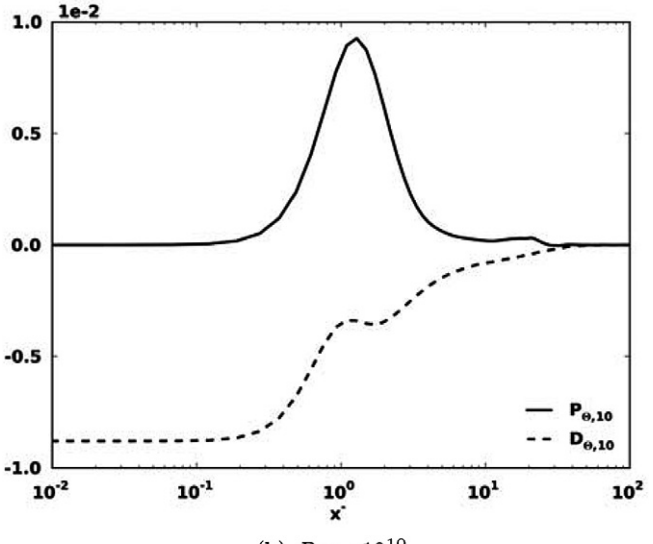

(b) $Ra = 10^{10}$

Fig. 8. Temperature variance production (P_Θ) and dissipation (D_Θ) rates at $x_2 = +0.3$ for $Ra = 10^9$, 10^{10}.

even unstable stratified in the neighbourhood. About the viscous dissipation terms D, they are maximum at the wall and rapidly decrease before $x^- = 1$ even if D_{10} remains larger than D_9 and comparable with G_{10} further deep in the core of the cavity. This is a relevant result which clearly shows the limits of the usual RANS $k-\epsilon$ models (tuned and well tested in forced flows between parallel plates for instance) when applied to turbulent natural convective flows where the regions of high fluctuating intensity and high dissipation rates are distant and the two quantities appear rather uncorrelated.

Finally the temperature variance production and dissipation terms, written as

$$P_\Theta = -2\langle u_i'\Theta'\rangle \frac{\partial\langle\Theta\rangle}{\partial x_i}, \tag{20}$$

and

$$D_\Theta = -2Pr\left\langle \frac{\partial\Theta'}{\partial x_i}\frac{\partial\Theta'}{\partial x_i}\right\rangle, \tag{21}$$

are plotted in Fig. 8 as a function of x^- for the two different Rayleigh numbers. Unlike the production terms P that appear in Eq. (19), the temperature variance production term P_Θ is positive for both Rayleigh numbers even if it approaches zero for $x^- \approx 7.5$ at $Ra = 10^9$ because of the almost neutral stratification mentioned before. Finally, D_Θ becomes really important only at $Ra = 10^{10}$ and close to the wall.

Table 5
Particle tracking computational parameters: Rayleigh number Ra_H, total number of particles injected N_p, particle diameter d_p, particle density ρ_w, particle Stokes number St, integration time step Δt, final time t_f.

Ra	N_p	d_p (μm)	ρ_w (kg m^{-3})	St	Δt	t_f
10^9	10^5	15	1000	1.26×10^{-3}	5.00×10^{-4}	134
	10^5	25	1000	3.50×10^{-3}	5.00×10^{-4}	160
	10^5	35	1000	6.86×10^{-3}	1.00×10^{-3}	160
10^{10}	10^5	15	1000	8.59×10^{-4}	1.00×10^{-4}	160
	10^5	25	1000	2.39×10^{-3}	1.00×10^{-4}	160
	10^5	35	1000	4.68×10^{-3}	1.00×10^{-4}	160

Please cite this article in press as: Puragliesi, R., et al. DNS of buoyancy-driven flows and Lagrangian particle tracking in a square cavity at high Rayleigh numbers. Int. J. Heat Fluid Flow (2011), doi:10.1016/j.ijheatfluidflow.2011.06.007

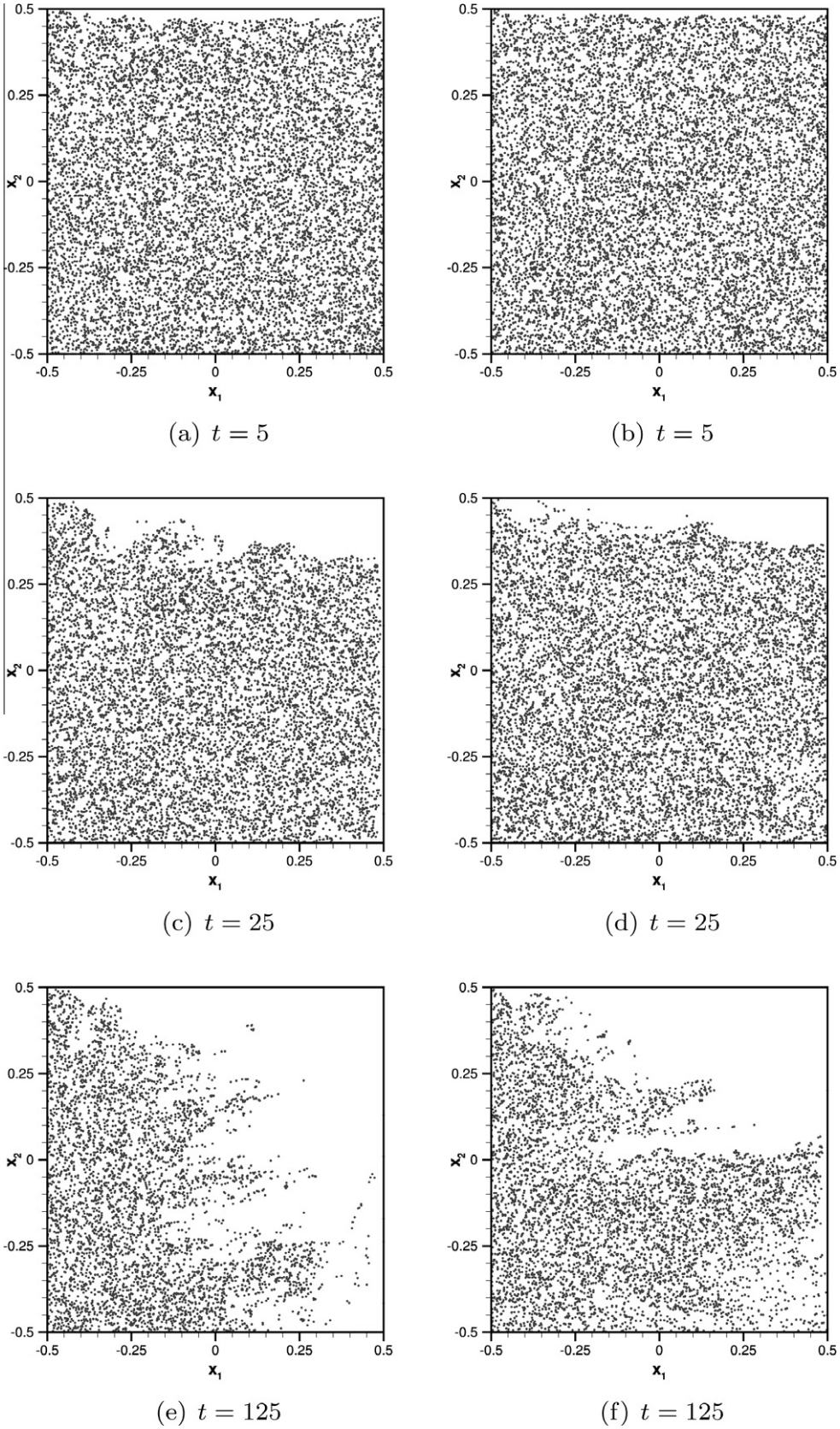

Fig. 9. Three instantaneous snapshots of particle locations at time $t = 5, 25, 125$ for diameter $d_p = 15$ [μm]. On the left column the case for $Ra = 10^9$, on the right the case for $Ra = 10^{10}$.

Please cite this article in press as: Puragliesi, R., et al. DNS of buoyancy-driven flows and Lagrangian particle tracking in a square cavity at high Rayleigh numbers. Int. J. Heat Fluid Flow (2011), doi:10.1016/j.ijheatfluidflow.2011.06.007

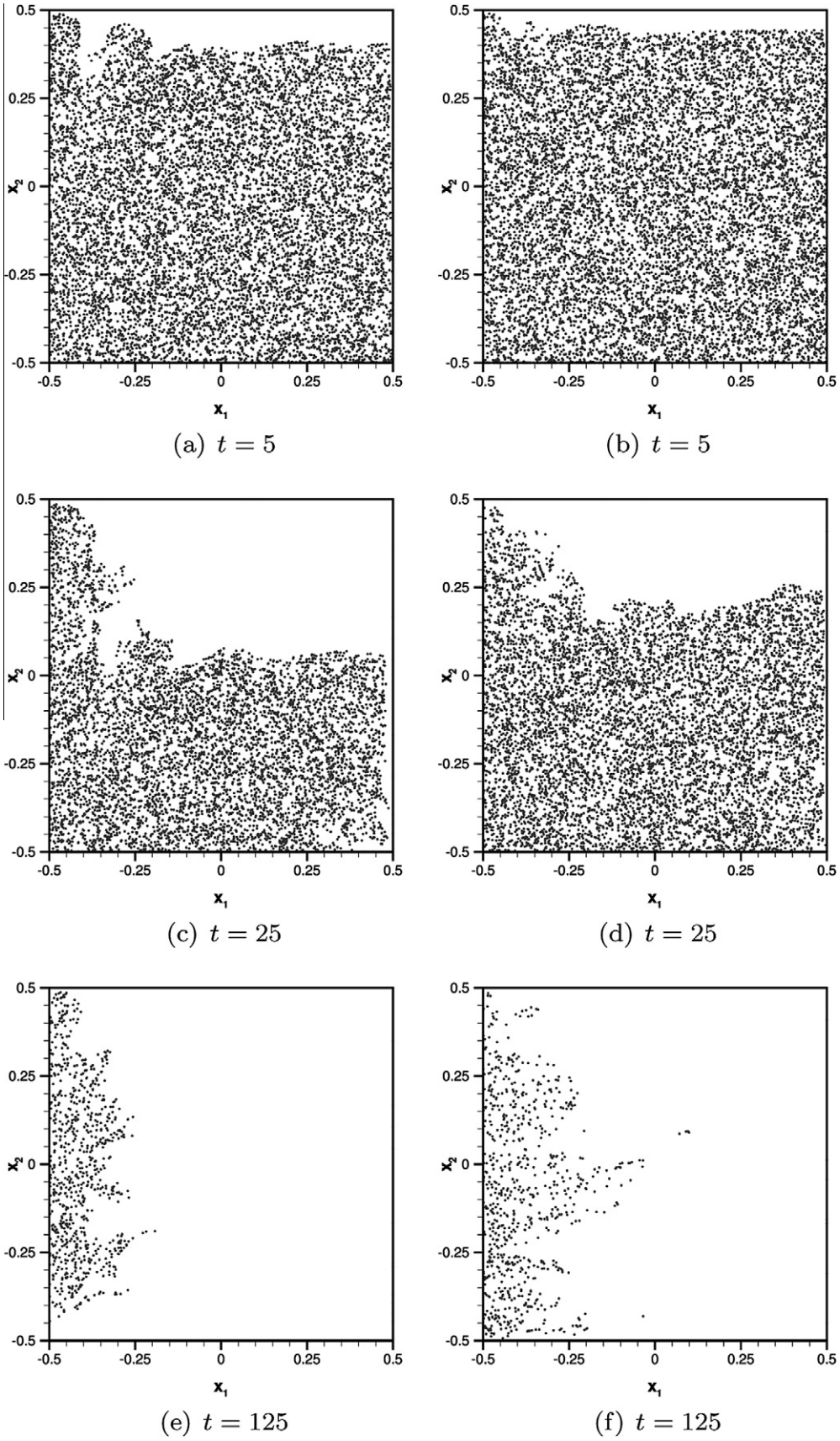

Fig. 10. Three instantaneous snapshots of particle locations at time $t = 5, 25, 125$ for diameter $d_p = 25$ [μm]. On the left column the case for $Ra = 10^9$, on the right the case for $Ra = 10^{10}$.

Please cite this article in press as: Puragliesi, R., et al. DNS of buoyancy-driven flows and Lagrangian particle tracking in a square cavity at high Rayleigh numbers. Int. J. Heat Fluid Flow (2011), doi:10.1016/j.ijheatfluidflow.2011.06.007

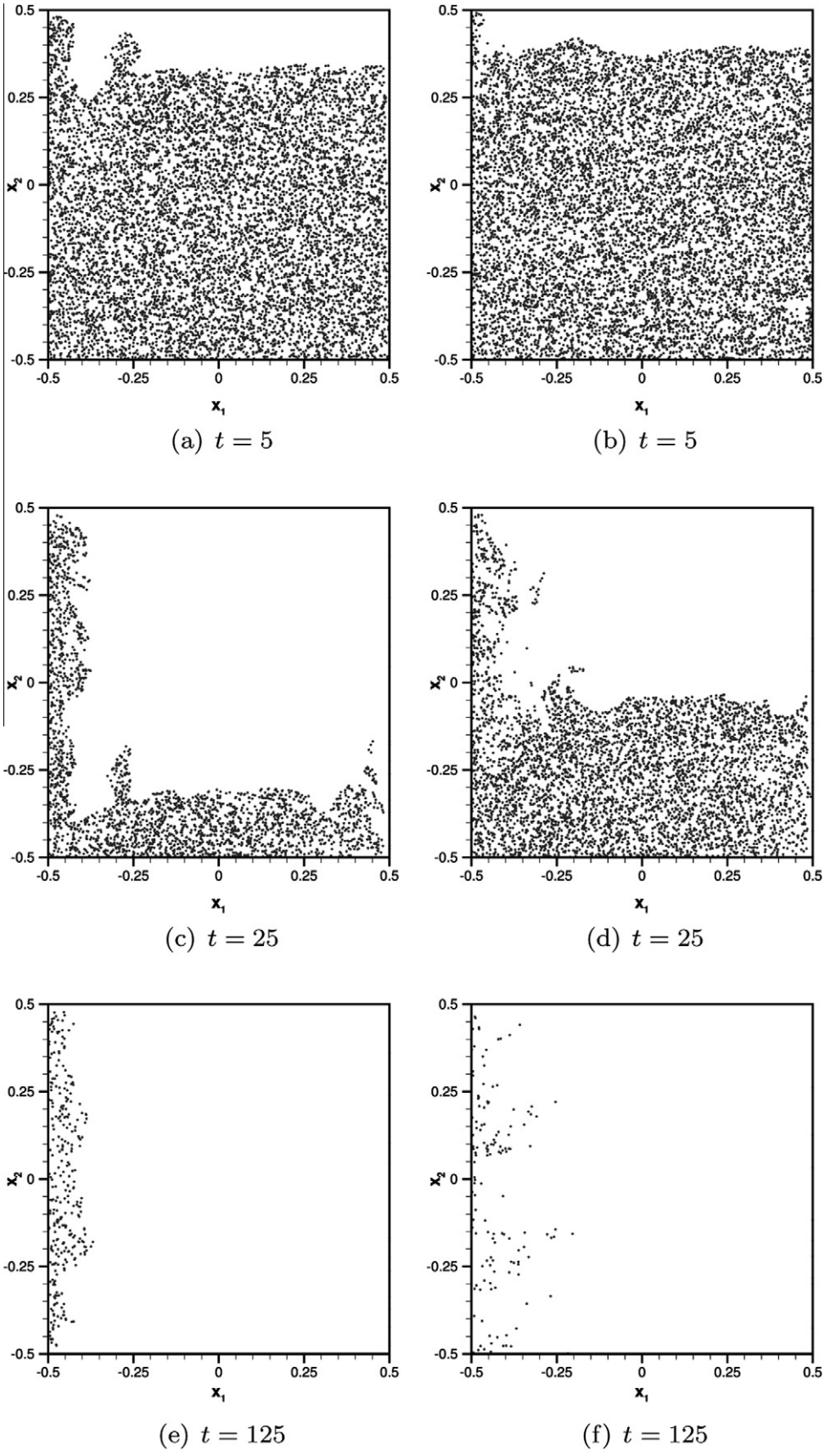

Fig. 11. Three instantaneous snapshots of particle locations at time $t = 5, 25, 125$ for diameter $d_p = 35$ [μm]. On the left column the case for $Ra = 10^9$, on the right the case for $Ra = 10^{10}$.

Please cite this article in press as: Puragliesi, R., et al. DNS of buoyancy-driven flows and Lagrangian particle tracking in a square cavity at high Rayleigh numbers. Int. J. Heat Fluid Flow (2011), doi:10.1016/j.ijheatfluidflow.2011.06.007

3.2. Dispersed phase

3.2.1. Particle deposition

After the flow has reached a statistical steady-state, three different sets of aerosol particles, each one composed by $N_p = 10^5$ pointwise solid spheres with diameter d_p and density ρ_w (Table 5), have been injected at random positions into the cavity domain, at $Ra = 10^9$, 10^{10}. The particle initial slip velocity is set to zero ($\mathbf{u} - \mathbf{v}_p = \mathbf{0}$). In Fig. 9–11 instantaneous snapshots of particle locations are provided for the tree different sets and the two regimes $Ra = 10^9$, 10^{10} at time $t = 5$, 25, 125. For each particle diameter an increase of the Rayleigh number corresponds to a slower rate of deposition. The reason is twofold: at higher Rayleigh numbers the height of the cavity increases so that particles of the same size, initially at the top wall, need to cover a larger distance before settling; due to the choice of the adimensionalization, the relaxation time (Table 5) becomes smaller in comparison with the scaling time used for the fluid and consequently particles behave more like tracers. It is reasonable to think that the large structures (those comparable with the cavity characteristic size H) become larger and persist longer at high Rayleigh number. This suggests that particles of the same size are strongly affected by the presence of these larger structures, and in particular the particle inertia becomes less important with respect to the drag force. It is important to stress that this counter intuitive behaviour is only due to the choice of the reference scales. For particles dispersed in forced flows the reference scales are based on the turbulence structures (much smaller than the large scales considered here) and an increment of the Reynolds number directly reflects in smaller length- and shorter time-scales leading to larger particle Stokes numbers (i.e. particle inertia becomes relevant with respect to the drag force). A proper scaling linked to turbulence quantities has not been found in the DHC configuration (neither based on the Kolmogorov scale due to the strong decoupling of the turbulent kinetic energy and its dissipation rate (Trias et al., 2010), nor based on the friction velocity since the shear stress varies along the active walls) but it would be auspicious.

As expected, at the same Rayleigh number it appears that bigger particles deposit faster than the smaller ones. Moreover, for all the cases examined, the cold side (right vertical wall, Fig. 10c for instance) becomes free of particles in a relative short time since drag and gravity forces drive them downward. At the hot wall a large recirculation pattern is visible and particles remain suspended because of the vertical hot jet. This latter result finds confirmation in the work of Yarin et al. (1996) even if the experimental conditions differ from those used in the present study. It is important to note that for the investigated diameters, no particles are reintroduced in the cold boundary layer from the upper region neither are able to diffuse inside the cold laminar boundary layer from the core. A net distinction (resembling to *free surface*) between the region occupied by particles in the core and the fluid phase at the top of the cavity can be observed during the sedimentation process. Its wavy profile is indeed induced by travelling internal gravity waves in the core, though the presence of the latter is overall negligible for the deposition process itself. Moreover, almost periodic particle ejections are encountered, for instance in Fig. 9e. These structures extend deeply in the core, depending on the Stokes number, thanks to the action of the unsteady hook-like structure and the weak horizontal wind.

Time histories of suspended particle fractions P_f for the three different diameters are presented in Fig. 12 for the two different Rayleigh numbers. For medium and large particle sizes (Fig. 12b and c) P_f shows clearly two different time behaviours: during the first instants we observe high and almost constant deposition rates (linear trend in the figures); later on, the sedimentation continues with very low deposition rates. The instant when the deposition

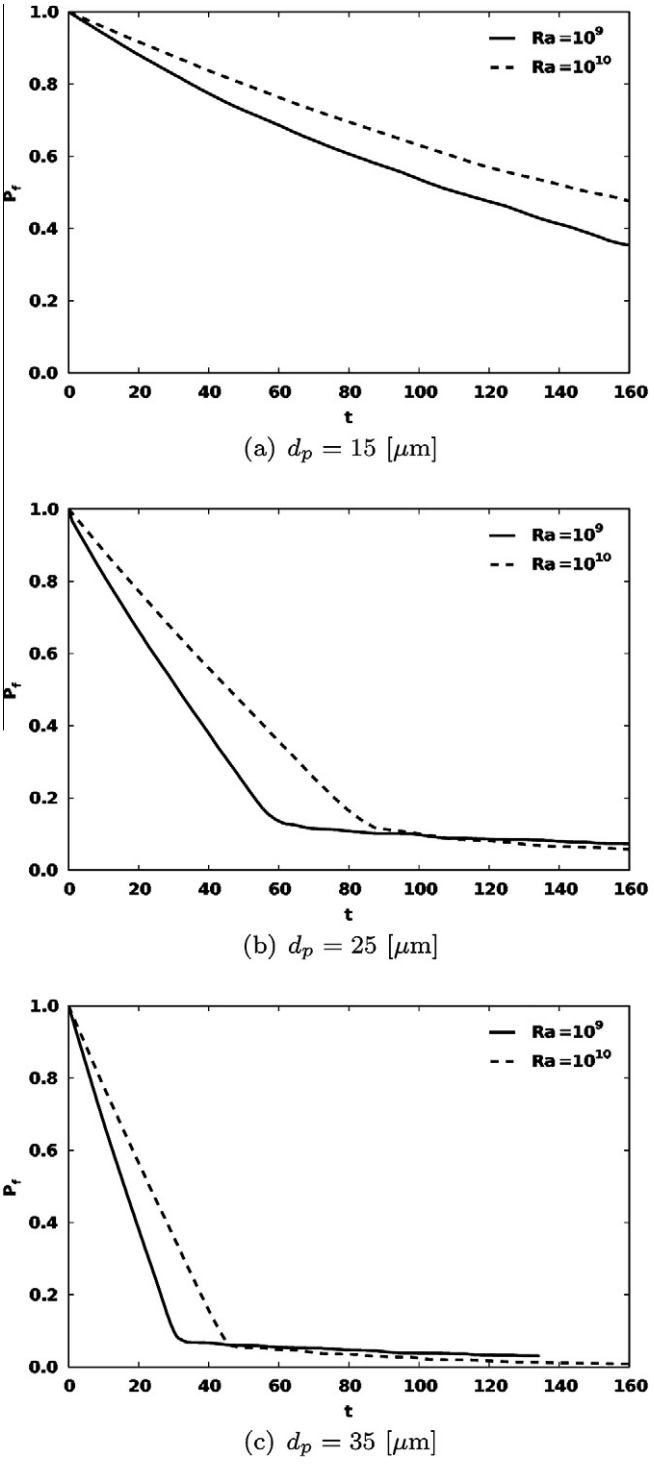

Fig. 12. Suspended particle fraction time histories for $Ra = 10^9$, 10^{10}: (a) $d_p = 15$ [μm], (b) $d_p = 25$ [μm], (c) $d_p = 35$ [μm].

Table 6
Theoretical settling times t_{th} for the three sets of particles for $Ra = 10^9$, 10^{10}.

Ra	t_{th}		
	$d_p = 15$ [μm]	$d_p = 25$ [μm]	$d_p = 35$ [μm]
10^9	163.96	59.03	30.12
10^{10}	240.63	86.49	44.17

Please cite this article in press as: Puragliesi, R., et al. DNS of buoyancy-driven flows and Lagrangian particle tracking in a square cavity at high Rayleigh numbers. Int. J. Heat Fluid Flow (2011), doi:10.1016/j.ijheatfluidflow.2011.06.007

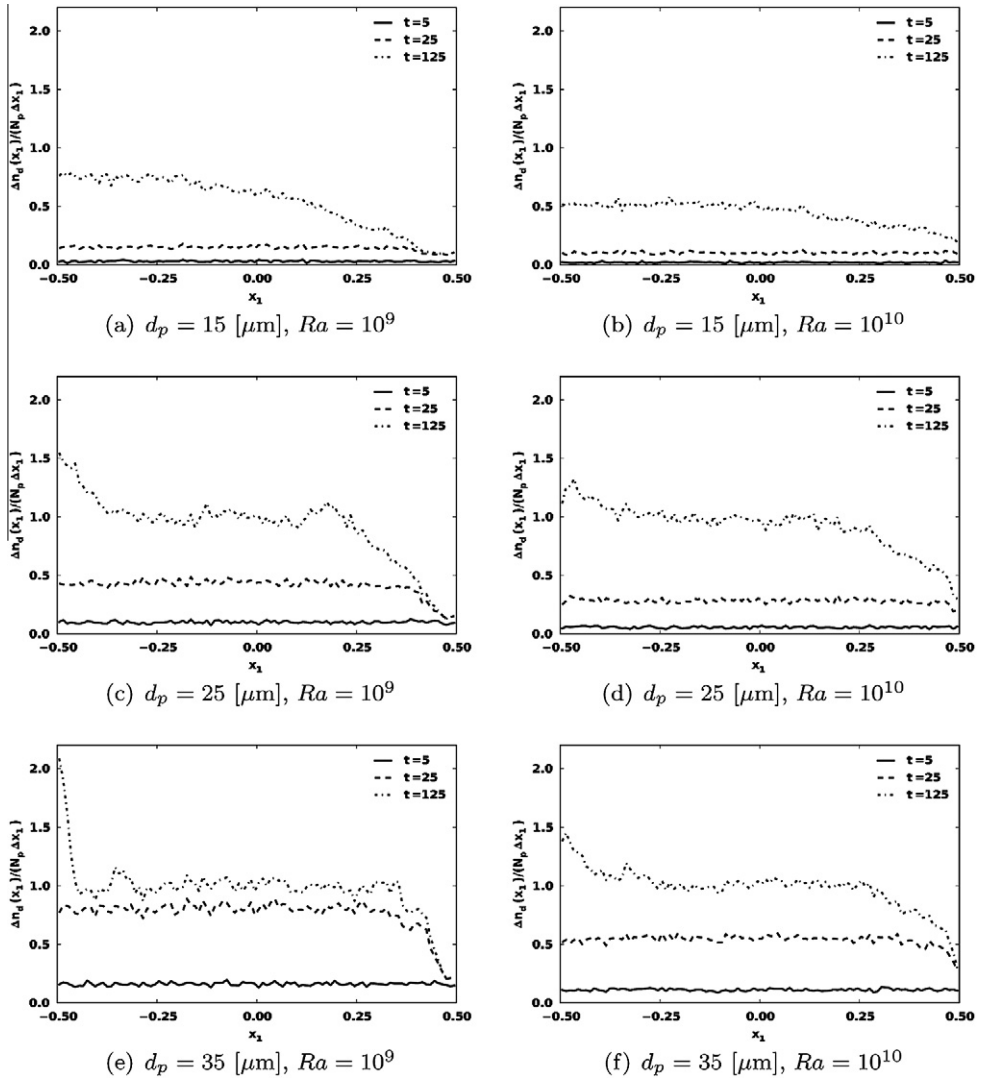

Fig. 13. Normalized concentration profiles of deposited particles at the bottom wall for three sets of particles at time $t = 5, 25, 125$ and $Ra = 10^9, 10^{10}$. (a and b) $d_p = 15$ [μm], (c and d) $d_p = 25$ [μm], (e and f) $d_p = 35$ [μm].

rate changes dramatically is compatible with the time needed by a particle to cover the distance H (Table 6) with the terminal velocity determined by imposing the balance between the buoyancy and the drag force in a quiescent environment at the reference temperature and pressure (i.e. $\mathbf{u} = \mathbf{0}$ and $\Theta = 0$). It is easy to demonstrate that the dimensionless theoretical settling time is equal to

$$t_{th} = \frac{\Delta\mathscr{T}}{PrSt(1-\mathscr{D})}. \tag{22}$$

After this consideration, it is possible to say that, during the first instants, the deposition of medium and big particles is basically driven uniquely by gravitation. The constant settling rate is intrinsically linked to the terminal velocity $\mathbf{v}_T = -PrSt(1-\mathscr{D})/\Delta\mathscr{T}\,\mathbf{e}_2$, assumed constant the concentration measured following the vertical motion of the particles injected in the core. For the smallest particle set (Fig. 12a) the first linear region is not truly detectable. It is clear that the small particles in the core are much more influenced by the weak horizontal wind and by the mixing induced by the hot jet and the hook-like structure. This yields the linear trend to vanish. However, it must be said that the integration time for the smallest size is unluckily too short to be able to show the sharp bent at $t \approx t_{th}$.

For the three different particle sets, in Fig. 13 are shown three instantaneous ($t = 5$, 25, 125) normalized concentration profiles of deposited particles at the bottom wall for $Ra = 10^9$, 10^{10}. The normalized concentration profile is defined by $\Delta n_d(x_1)/(N_p \Delta x_1)$ where $\Delta n_d(x_1)$ is the number of particles deposited in a interval of length Δx_1 centred in x_1. We can notice that the long term deposition profile is always non-uniform along the bottom wall. Indeed the presence of the weak horizontal wind and the lower recirculation pocket modifies the deposition patterns, and an almost uniform profile is recorded in each case under investigation at the early stages. This is because the initial conditions (i.e. injection position) and the gravity rule the deposition process everywhere along the bottom wall during the first instants. When the initial conditions are no longer important, an absence of particles is encountered close to the cold wall. The particles coming from the cold boundary layer diffuse in the lower part of the core thanks to the action of the hook-like structure, whereas those coming from outside the cold boundary layer are unable to directly settle at the bottom wall because of the centrifugal effect of the recirculation pocket. Long time deposition profiles tend to show a remarkable peak at the hot wall ($x_1 = -0.5$) because the horizontal wind in the lower part of the cavity drives particles from the cold side to

Please cite this article in press as: Puragliesi, R., et al. DNS of buoyancy-driven flows and Lagrangian particle tracking in a square cavity at high Rayleigh numbers. Int. J. Heat Fluid Flow (2011), doi:10.1016/j.ijheatfluidflow.2011.06.007

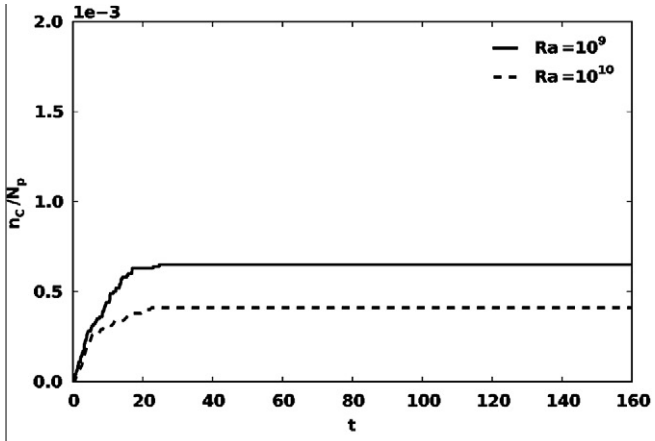

(a) $d_p = 15$ [μm]

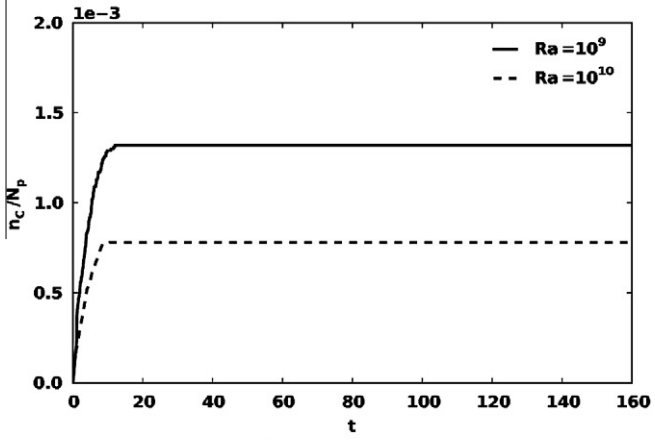

(b) $d_p = 25$ [μm]

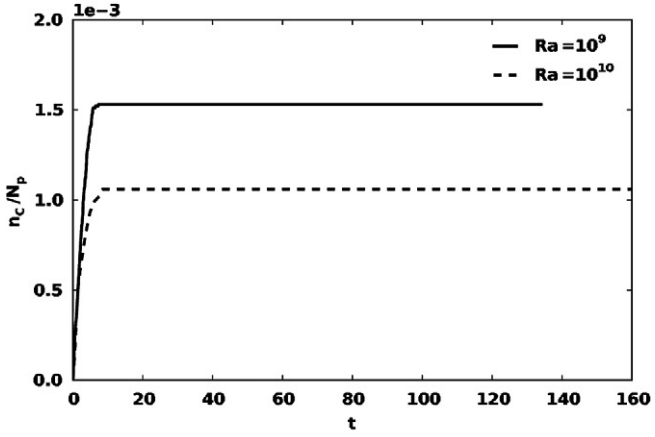

(c) $d_p = 35$ [μm]

Fig. 14. Time histories of the particle number fraction deposited n_C/N_p at the cold wall for $Ra = 10^9$, 10^{10}. (a) $d_p = 15$ [μm], (b) $d_p = 25$ [μm], (c) $d_p = 35$ [μm].

the hot side and eventually they settle in the vicinity of the hot wall if the hot jet is not able to lift them. This is also true for particles that are ejected from the hot side in the core by the unsteady hook-like structure located in the top-left corner. Unlike the deposition process in a vertical channel that presents a constant deposition velocity (which depends on the particle size) (Reeks and Skyrme, 1976), in the present DHC it is possible to distinguish three different regions with different durations of sedimentation

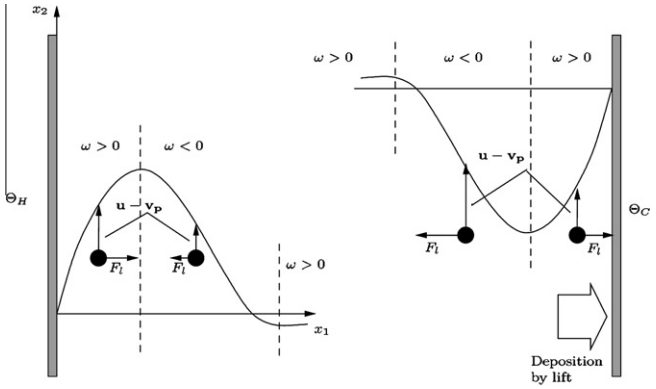

Fig. 15. Schematic representation of the effects induced by the lift force at the two active walls: hot wall on the left side, cold wall on the right side. The slip velocity is always directed upward due to the gravity acceleration which makes heavy particle moving faster than the fluid inside the cold boundary layer and slower inside the hot one. Moreover, the vertical velocity boundary layer can be divided in two zones with positive and negative vorticity. The joint action of these two effects together with the fact that as smaller is the Stokes number as lower gets the slip velocity, leads to different deposition velocities at the vertical cold wall, and avoids deposition at the hot one.

making more difficult the characterization of the settling process using a single quantity.

3.2.2. Influence of the lift and the thermophoretic forces

In the previous part the attention was focused on the particles that settle on the horizontal bottom surface but a very small particle fraction actually deposits on the vertical cold wall (all the other boundary surfaces are free of particles). In Fig. 14 the evolution of the particle number fraction n_C/N_p deposited at cold wall is presented for the three different sizes and the two Rayleigh numbers (n_C being the number of particles stuck on the cold surface). First of all, this deposition process ends after a very short time, suggesting that only particles which are initially injected in the extreme vicinity of the cold wall are able to hit the cold wall. Moreover, smaller particles have less tendency to deposit. Neglecting the small effect due to the rarefied distribution (i.e. particles are less dense), which slightly decreases the probability of a particle to hit the wall, it is possible to discard also the influence of the thermophoretic force since its contribution would instead induce a larger deposition for smaller Stokes numbers (see Eq. (13)). It can be deduced that the lift force is the major mechanism responsible for the removal at the cold wall (Marchioli et al., 2007). This latter result is valid for diameters of the order $O(10)$ micron and larger. On the other hand, Akbar et al. (2009) have demonstrated that the thermophoresis and the Brownian diffusion play a fundamental role for sub-micron particle deposition. A schematic representation of the mechanism that describes the particle deposition at the vertical cold wall induced by lift is illustrated in Fig. 15. Basically, the slip velocity (*i.e.* the relative velocity between the fluid and the particle) is always directed upward due to the gravity acceleration which makes heavy particle moving faster than the fluid inside the cold boundary layer and slower inside the hot one. Moreover, the vertical velocity boundary layer can be divided in two zones with positive and negative vorticity. The joint action of these two effects, together with the fact that as smaller is the Stokes number as lower gets the slip velocity, leads to different deposition velocities at the vertical cold wall, and avoids deposition over the hot one. As previously stated, small particles behave like tracers (the slip velocity tends to zero) and consequently also the magnitude of the lift force in Eq. (13) results smaller as lower is the final particle fraction deposited at the cold wall.

Please cite this article in press as: Puragliesi, R., et al. DNS of buoyancy-driven flows and Lagrangian particle tracking in a square cavity at high Rayleigh numbers. Int. J. Heat Fluid Flow (2011), doi:10.1016/j.ijheatfluidflow.2011.06.007

4. Conclusions

Two-dimensional direct numerical simulations of natural convective flows inside a square cavity filled with air and heated from the vertical sides at high Rayleigh numbers ($Ra = 10^9$, 10^{10}) and Lagrangian tracking of inertial particles have been performed.

The state-of-the-art of high-order Chebyshev pseudo-spectral method has been used for the discretization of the Navier–Stokes and energy transport equations. Very accurate first- and second-order statistics are provided for the velocity and temperature fields. The role of the mean pressure field in natural convective flows in presence of a stable stratified environment has been briefly discussed. Away from the active walls, the mean pressure distribution is intrinsically linked to the mean temperature field and its gradient balances the buoyancy force. The mixing produced by the chaotic flow at $Ra = 10^{10}$ strongly modifies both the averaged temperature and velocity fields, and it affects the transfer of momentum and heat at the wall. The production and the dissipation rates of turbulent kinetic energy (TKE) and temperature variance are discussed for the two Rayleigh numbers. A strong decoupling between the turbulent kinetic energy (high intensities are depicted inside the recirculating pockets) and the dissipation rate (high at the vertical walls) has been found. This peculiar behaviour is a major issue in turbulence modelling. A better match is registered for the temperature variance and its dissipation field. A different sustainment mechanism of the turbulent kinetic energy is also encountered for the two different Rayleigh numbers.

Concerning the sedimentation process of aerosol particles, a Lagrangian approach has been employed to track three sets of particles with different diameters $d_p = 15$, 25, 35 [μm] and density $\rho_w = 1000$ [kg/m^3]. A sixth-order Lagrange interpolation scheme and an explicit fourth-order Runge–Kutta integration formula have been employed. For diameters larger than 10 [μm] the particles deposit preferentially at the bottom wall in agreement with (Guentay et al., 2004). During the first instants, very large particles show high deposition rate, whereas for long times, low deposition rate is registered. This behaviour is not found for the particles with the smallest diameter investigated here since the weak horizontal wind largely affects their transport and inhibits the gravity drift. Particle recirculating loops occur along the whole height of the hot wall. This evidence is in agreement with the experimental results of Yarin et al. (1996). The thermophoretic and lift forces have been investigated looking at the fraction of particle that deposits at the cold wall (all the other surfaces are free of particles) and it is reasonable to conclude that their influence is negligible for the global deposition process of particles with diameter larger than 10 [μm].

The extension of the present analysis to fully three-dimensional turbulent DHC flow and Lagrangian particle tracking will be the object of future publications (Puragliesi, 2010).

Acknowledgements

This research has been funded by the ARTIST Consortium Project whose support is greatly acknowledged. The DNS data were obtained on Pleiades-2 cluster at EPFL-STI-IGM. E. Leriche greatly acknowledges the financial support of ERCOFTAC Visitors Program.

References

Akbar, M., Rahman, M., Ghiaasiaan, S., 2009. Particle transport in a small square enclosure in laminar natural convection. J. Aerosol Sci. 40, 747–761.

Allery, C., Beghein, C., Hamdouni, A., 2008. On investigation of particle dispersion by a POD approach. Int. Appl. Mech. 44, 110–119.

Ampofo, F., Karayannis, T., 2003. Experimental benchmark data for turbulent natural convection in an air filled square cavity. Int. J. Heat Mass Transfer 46, 3551–3572.

Balachandar, S., Maxey, M.R., 1989. Methods for evaluating fluid velocities in spectral simulations of turbulence. J. Comput. Phys. 83, 96–125.

Batoul, A., Khallouf, H., Labrosse, G., 1994. Une Méthode de Résolution Directe (Pseudo-Spectrale) du Problème de Stokes 2D/3D Instationnaire. Application à la Cavité Entrainée Carrée. C. R. Acad. Sci. Paris 319 (Série I), 1455–1461.

Bejan, A., 1984. Convection Heat Transfer. Wiley-Interscience.

Canuto, C., Hussaini, M.Y., Quarteroni, A., Zang, T.A., 1988. Spectral Methods in Fluid Dynamics. Springer Series in Computational Physics. Springer-Verlag, New-York.

Cherukat, P., McLaughlin, J.B., Dandy, D.S., 1999. A computational study of the inertial lift on a sphere in a linear shear flow field. Int. J. Multiphase Flow 25, 15–33.

Clément, B., Hanniet-Girault, N., Repetto, G., Jacquemain, D., Jones, A.V., Kissane, M.P., von der Hardt, P., 2003. LWR severe accident simulation: synthesis of the results and interpretation of the first Phebus FP experiment FPT0. Nucl. Eng. Des. 226, 5–82.

Deville, M., Fischer, P., Mund, E., 2002. High-Order Method for Incompressible Fluid Flow. Cambridge University Press, Cambridge.

Elghobashi, S., 1994. On predicting particle-laden turbulent flows. Appl. Sci. Res. 52, 309–329.

Elghobashi, S., Truesdell, G., 1992. Direct simulation of particle dispersion in a decaying isotropic turbulence. J. Fluid Mech. 242, 655–700.

Gatignol, R., 1983. The Faxén formulae for a rigid particle in an unsteady nonuniform Stokes flow. J. Mec. Theor. Appl. 1, 143–160.

Gelfgat, A.Y., 2004. Stability and slightly supercritical oscillatory regimes of natural convection in a 8:1 cavity:solution of the benchmark problem by a global Galerkin method. Int. J. Numer. Methods Fluids 44, 135–146.

Giusti, A., Lucci, F., Soldati, A., 2005. Influence of the lift force in direct numerical simulation of upward/downward turbulent channel flow laden with sufactant contaminated microbubbles. Chem. Eng. Sci. 60, 6176–6187.

Gottlieb, D., Orszag, S., 1977. Numerical Analysis of Spectral Methods: Theory and Applications. SIAM-CBMS, Philadelphia.

Gouesbet, G., Berlemont, A., 1998. Eulerian and Lagrangian approaches for predicting the behaviour of discrete particles in turbulent flows. Prog. Energy Combust. Sci. 25, 133–159.

Gray, D.D., Giorgini, A., 1976. The validity of the Boussinesq approximation for liquids and gases. Int. J. Heat Mass Transfer 19, 545–551.

Guentay, S., Suckow, D., Dehbi, A., Kapulla, R., 2004. ARTIST: introduction and first results. Nucl. Eng. Des. 231, 109–120.

Haldenwang, P., Labrosse, G., Abboudi, S., Deville, M., 1984. Chebyshev 3D spectral and 2D pseudospectral solvers for the Helmholtz equation. J. Comput. Phys. 55, 115–128.

Henkes, R.A.W.M., Hoogendoorn, C.J., 1990. On the stability of the natural convection flow in a square cavity heated from the side. Appl. Sci. Res. 47, 26. Anglais.

Janssen, R.J.A., Henkes, R.A.W.M., 1996. Instabilities in three-dimensional differentially-heated cavities with adiabatic horizontal walls. Phys. Fluids 8, 62–74.

Karniadakis, G.E., Israeli, M., Orszag, S.A., 1991. High-order splitting methods for the incompressible Navier–Stokes equations. J. Comput. Phys. 97, 414–443.

Kissane, M.P., 2008. On the nature of aerosols produced during a severe accident of a water-cooled nuclear reactor. Nucl. Eng. Des. 238, 2792–2800.

Kontomaris, K., Hanratty, T.J., McLaughlin, J.B., 1992. An algorithm for tracking fluid particles in a spectral simulation of turbulent channel flow. J. Comput. Phys. 103, 231–242.

Kurose, R., Komori, S., 1999. Drag and lift forces on a rotating sphere in a linear shear flow. J. Fluid Mech. 384, 183–206.

Labrosse, G., 1993. Compatibility conditions for the Stokes system discretized in 2D Cartesian domains. Comput. Methods Appl. Mech. Eng. 106, 353–365.

Le Quéré, P., 1991. Accurate solutions to the square thermally driven cavity at high Rayleigh number. Comput. Fluids 20 (1), 29–41.

Le Quéré, P., Behnia, M., 1998. From onset of unsteadiness to chaos in a differentially heated square cavity. J. Fluid Mech. 359, 81–107.

Le Quéré, P., Masson, R., Perrot, P., 1992. A Chebyshev collocation algorithm for 2D non-Boussinesq convection. J. Comput. Phys. 103, 320–334.

Leong, W., Hollands, K., Brunger, A., 1998. On a physically-realizable benchmark problem in internal natural convection. Int. J. Heat Mass Transfer 41, 3817–3828.

Leong, W.H., Hollands, K.G.T., Brunger, A.P., 1999. Experimental Nusselt number for a cubical-cavity benchmark problem in natural convection. Int. J. Heat Mass Transfer 42, 1979–1989.

Leriche, E., Labrosse, G., 2000. High-order direct Stokes solvers with or without temporal splitting: numerical investigations of their comparative properties. SIAM J. Sci. Comput. 22 (4), 1386–1410.

Leriche, E., Perchat, E., Labrosse, G., Deville, M., 2006. Numerical evaluation of the accuracy and stability properties of high-order direct Stokes solvers with or without temporal splitting. J. Sci. Comput. 26, 25–43.

Lynch, R., Rice, J., Thomas, D., 1964. Direct solution of partial difference equations by tensor product methods. Numer. Math. 6, 185–199.

Mamun, M.A.H., Leong, W.H., Hollands, K.G.T., Johnson, D.A., 2003. Cubical-cavity natural-convection benchmark experiments: an extension. Int. J. Heat Mass Transfer 46 (19), 3655–3660.

Marchioli, C., Picciotto, M., Soldati, A., 2007. Influence of gravity and lift on particle velocity statistics and transfer rates in turbulent vertical channel flow. Int. J. Multiphase Flow 33, 227–251.

Please cite this article in press as: Puragliesi, R., et al. DNS of buoyancy-driven flows and Lagrangian particle tracking in a square cavity at high Rayleigh numbers. Int. J. Heat Fluid Flow (2011), doi:10.1016/j.ijheatfluidflow.2011.06.007

Mergui, S., Penot, F., 1996. Convection naturelle en cavité carrée différentiellement chauffée: investigation expérimentale à $Ra = 1.69 \times 10^9$. Int. J. Heat Mass Transfer 39, 563–574.

Mergui, S., Penot, F., 1997. Analyse des vitesse et température de l'air en convection naturelle dans une cavité carrée différentiellement chauffée à $Ra = 1.69 \times 10^9$. Int. J. Heat Mass Transfer 40, 3427–3441.

Niemela, J., Sreenivasan, K., 2006. The use of cryogenic helium for classical turbulence: promises and hurdles. J. Low Temp. Phys. 143, 163–212.

Paolucci, S., Chenoweth, D.R., 1989. Transition to chaos in a differentially heated vertical cavity. J. Fluid Mech. 201, 379–410.

Peng, S., Davidson, L., 2001. Large eddy simulation for turbulent buoyant flow in a confined cavity. Int. J. Heat Fluid Flow 22 (3), 323–331.

Penot, F., Skurtys, O., Saury, D., 2010. Preliminary experiments on the control of natural convection in differentially-heated cavities. Int. J. Therm. Sci. 49, 1911–1919.

Podvin, B., Le Quéré, P., 2001. Low-order models for the flow in a differentially heated cavity. Phys. Fluids 13, 3204–3214.

Puragliesi, R., 2010. Numerical investigation of particle-laden thermally driven turbulent flows in enclosure. Ph.D. thesis, No. 4600, École Polytechnique Fédérale de Lausanne, Lausanne.

Ravi, M.R., Henkes, R.A.W.M., Hoogendoorn, C.J., 1994. On the high-Rayleigh-number structure of steady laminar natural-convection flow in a square enclosure. J. Fluid Mech. 262, 325–351.

Ravnik, J., Skerget, L., Hribersek, M., 2006. Two-dimensional velocity-vorticity based LES for the solution of natural convection in a differentially heated enclosure by wavelet transform based BEM and FEM. Eng. Anal. Boundary Elem. 30, 671–686.

Reeks, M., Skyrme, G., 1976. The dependence of particle deposition velocity on particle inertia in turbulent pipe flow. J. Aerosol Sci. 7, 485–495.

Soldati, A., 2005. Particles turbulence interactions in boundary layers. Z. Angew. Math. Mech. 85, 683–699.

Suslov, S.A., Paolucci, S., 1995. Stability of natural convection flow in a tall vertical enclosure under non-Boussinesq condition. Int. J. Heat Mass Transfer 38, 2143–2157.

Suslov, S.A., Paolucci, S., 1997. Nonlinear analysis of convection flow in a tall vertical enclosure under non-Boussinesq conditions. J. Fluid Mech. 344, 1–41.

Talbot, L., Cheng, R.K., Schefer, R.W., Willis, D.R., 1980. Thermophoresis of particles in a heated boundary-layer. J. Fluid Mech. 101, 737–758.

Tiang, Y., Karayiannis, T., 2000a. Low turbulence natural convection in an air filled square cavity, Part I: the thermal and fluid flow fields. Int. J. Heat Mass Transfer 43, 849–866.

Tiang, Y., Karayiannis, T., 2000b. Low turbulence natural convection in an air filled square cavity, Part II: turbulence quantities. Int. J. Heat Mass Transfer 43, 867–884.

Trias, F., Gorobets, A., Soria, M., Oliva, A., 2010. Direct numerical simulation of a differentially heated cavity of aspect ratio 4 with Rayleigh numbers up to 10^{11} – Part II: heat transfer and flow dynamics. Int. J. Heat Mass Transfer 53, 674–683.

Trias, F., Soria, M., Oliva, A., Pérez-Segarra, C., 2007. Direct numerical simulation of two- and three-dimensional turbulent natural convection flows in a differentially heated cavity of aspect ratio 4. J. Fluid Mech. 586, 259–293.

Tric, E., Labrosse, G., Betrouni, M., 2000. A first incursion into the 3D structure of natural convection of air in a differentially heated cubic cavity, from accurate numerical solutions. Int. J. Heat Mass Transfer 43, 4043–4056.

Tsorng, S., Capart, H., Lai, J., Young, D., 2006. Three-dimensional tracking of the long time trajectories of suspended particles in a lid-driven cavity flow. Exp. Fluids 40, 314–328.

Tsorng, S.J., Capart, H., Lo, D., Lai, J.S., Young, D.L., 2008. Behaviour of macroscopic rigid spheres in lid-driven cavity flow. Int. J. Multiphase Flow 34, 76–101.

de Vahl Davis, G., 1983. Natural convection of air in a square cavity: a benchmark numerical solution. Int. J. Numer. Methods Fluids 3 (3), 249–264.

de Vahl Davis, G., Jones, I.P., 1983. Natural-convection in a square cavity – a comparison exercise. Int. J. Numer. Methods Fluids 3 (3), 227–248.

Xin, S., Le Quéré, P., 2002. An extended Chebyshev pseudo-spectral benchmark for the 8:1 differentially heated cavity. Int. J. Numer. Methods Fluids 40, 981–998.

Yarin, A.L., Kowalewski, T.A., Hiller, W.J., Koch, S., 1996. Distribution of particles suspended in convective flow in differentially heated cavity. Phys. Fluids 8, 1130–1140.

Please cite this article in press as: Puragliesi, R., et al. DNS of buoyancy-driven flows and Lagrangian particle tracking in a square cavity at high Rayleigh numbers. Int. J. Heat Fluid Flow (2011), doi:10.1016/j.ijheatfluidflow.2011.06.007